A new isotropic hyper-elasticity model for enhancing the rate of convergence of Mohr-Coulomb-like constitutive models and application to shallow foundations and trapdoors

L.P. Argani[a,b,*], A. Gajo[a]

[a] *Department of Civil, Environmental & Mechanical Engineering, University of Trento, via Mesiano 77, I-38123 Trento, Italy*
[b] *Department of Mathematical Sciences, University of Liverpool, Mathematical Sciences Building, Liverpool L69 7ZL, UK*

Abstract

A new hyper-elastic formulation is proposed for improving the convergence of Mohr-Coulomb-like constitutive models at small stresses, when the convergence problems come from the vicinity to the apex of the yield surface and the elastic predictor can lay in a region in which the yield surface is not defined. The proposed hyper-elastic formulation avoids stress states with tensile mean pressures and provides shear and bulk stiffnesses increasing with the square root of mean stress, as typically occurs in granular soil. The new model is applied to two typical engineering problems: a centred-loaded, superficial foundation and the active and passive trapdoor problem. The numerical results are compared with upper and lower bound solutions, showing the reliability of FEM results. In addition, FEM analyses highlight some peculiar aspects of soil-foundation interaction which are usually neglected in the current engineering practice of foundation design.

Keywords: constitutive modelling, soil-structure interaction, hyper-elastic formulation, finite element analysis, small stress

1. Introduction

In engineering practice the empirical approach of estimating the factor of safety through a reduction of soil strength parameters in finite element (FEM) or finite difference (FD) analyses is more and more often used. The limit load in fact is easily deduced from the loss of the numerical convergence. Typically these FEM or FD analyses are performed with an elastic-perfectly plastic, Mohr-Coulomb model.

This approach is based on two assumptions: a) the lack of convergence is related to the formation of a rupture mechanism and not to a pure convergence problem of the numerical code, b) the rupture mechanism evaluated with FEM or FD methods provides a reliable estimate of the limit load as compared to rigorous theoretical evaluations, for instance based on the theorems of limit analysis.

Unfortunately none of the above assumptions is usually verified. In fact, the convergence difficulties due to the corners and the vertex of the Mohr-Coulomb yield surface pose great numerical problems, especially for stress states close to the vertex of the Mohr-Coulomb yield surface. A typical example is the evaluation of the limit load of a shallow foundation with null embedment depth, for which the lack of numerical convergence typically occurs at negligible applied loads (well below the theoretical limit load) and is entirely related to numerical problems and not to the formation of a rupture mechanism.

In addition, it is well known that FEM and FD numerical models are affected by a pathological mesh dependence in which the band thickness and rupture mechanisms are affected by mesh size and orientation. As a result, the rupture mechanism and the limit load resulting from FEM calculation might be much different from theoretical expectations.

In the literature, different continuous approximations of the Mohr-Coulomb yield surface were proposed [36, 22, 27], which are not however completely sufficient to solve the numerical problems occurring at the yield surface vertex. Among the methods proposed in the literature for enhancing the convergence of Mohr-Coulomb constitutive models, it is worth mentioning the method proposed by La Gioia & Panteghini [23, 14], where a novel formulation is introduced to approximate a broad class of failure criteria (i.e. Drucked-Prager, Mohr-Coulomb, Matsuoka-Nakai, etc.) by means of a C2 continuous general expression for the yield function: a very limited number of parameters allow to swap from the approximation of one of the classical yield surface to that of another one, while preserving C2 continuity. Moreover, they introduced an ad-hoc algorithm to improve the efficiency of the implementation of the aforementioned C2 continuous yield function.

*Corresponding author at: Department of Civil, Environmental & Mechanical Engineering, University of Trento, via Mesiano 77, I-38123 Trento, Italy. E-mail address: luca.argani@unitn.it

It is worth emphasizing that the numerical problems related to low mean stress state in the vicinity of the vertex of the Mohr-Coulomb yield surface are found also in all Mohr-Coulomb-like constitutive models, like Severn-Trent [6, 7] and Sanisand models [16, 32]. In fact, these constitutive models are based on a yield surface with a rounded deviatoric section (thus eliminating the corners of the Mohr-Coulomb yield surface in the deviatoric plane), but the problems related to low mean stress state in the vicinity of the vertex of the yield surfaces may lead to great numerical difficulties. For instance, these numerical problems arise in the layers close to the ground surface when performing simulations of piles and sheet pile walls subjected to horizontal static or seismic loading. As a workaround, it is possible to represent the shallowest soil layer as a soft elastic material [25], thus eliminating the problems associated to the yield surface.

The aim of this work is to propose a new hyper-elastic formulation that is capable to describe the granular soil response at mean stress states of practical engineering relevance and, furthermore, is capable to enhance the numerical convergence in the case of extremely low mean stress states that are close to the vertex of Mohr-Coulomb-like yield surface. The numerical improvement is obtained through the fact that the proposed hyper-elastic formulation naturally prevents the elastic predictor to lay in regions where the yield function is not defined. In particular, notwithstanding that the proposed hyper-elastic formulation is obtained through the combination of two existing formulations, the resulting free energy density function is sufficiently smooth to ensure good convergence properties. It is important to emphasise that the proposed elasticity law can be implemented in any classical elastic-plastic constitutive model, based on a Mohr-Coulomb-like yield criterion.

The text is organised as follows. The proposed hyper-elastic formulation is discussed in Section 2, where typical model simulations are presented. Section 3 presents the whole constitutive model, which is implemented in a user defined subroutine (UMAT) for Abaqus Unified FEA (Dassault Systèmes®), with ad-hoc numerical improvements. In particular, the proposed hyper-elastic formulation has been incorporated in a continuous approximation of the Mohr-Coulomb yield surface proposed in the literature [1].

In the final part of this work (Sections 4 and 5), the limit loads computed numerically are compared with the upper and lower bound solutions for the two classical examples of a centred-loaded, shallow foundation and active and passive trapdoor problems. In particular, the effects induced by triangular and quadrangular meshes with different refinement levels for a shallow foundation are investigated in detail in Section 4. Section 5 is focussed on the evaluation of the limit load for the shallow foundation and for the active and passive trapdoor, which are challenging problems related to engineering applications. In particular, for the shallow foundation problem the solution is obtained by means of the proposed formulation as well as of another commercial code which exploits the Discontinuity Layout Optimization technique (DLO) in order to provide a comparison of the performance. These comparisons allow to appreciate the features of the proposed framework and will shed new lights on the reliability of FEM computations for the limit load evaluation, when a simple elastic-perfectly plastic Mohr-Coulomb model is employed, as often done in engineering practice. Moreover, these analyses highlight some peculiar aspects of soil-foundation interaction which are usually neglected in the current engineering design of foundations (Section 5). Conclusions are finally drawn in Section 6.

2. The new hyper-elasticity law

The key concept of the new hyper-elasticity law for enhancing the convergence of Mohr-Coulomb criterion at low mean pressures is to avoid that the elastic predictor lays in a region where the yield surface is not defined, namely where the mean stress is positive (i.e. in tension for $c' = 0$). In this way, all of the challenging numerical problems of return mapping towards the yield surface are avoided.

According to this concept, at first glance the elasticity law of Cam-Clay model may appear to be a useful means, because through the exponential relationship between the volumetric strain and the mean stress, a null mean stress is obtained only at infinitely large (compressive) volumetric strains and a positive (tensile) mean stress can never be obtained. Unfortunately, the classical Cam-Clay elasticity law is based on a constant shear stiffness (beside the varying tangent bulk stiffness), which may lead to very large or negligibly small ratios between shear and bulk elastic tangent stiffnesses, thus causing numerical difficulties. Gajo & Bigoni [5] have proposed a hyper-elastic model in which both the shear and the bulk stiffnesses increase with the mean stress, thus avoiding the numerical problems of the above mentioned Cam-Clay elasticity model.

As a result, taking inspiration from Cam-Clay elasticity model and Gajo & Bigoni [5] hyper-elastic formulation, we propose the following free-energy density function φ, obtained as a smooth combination of these two elasticity models

$$\varphi(\boldsymbol{\varepsilon}^{\mathrm{e}}) = \begin{cases} \kappa\, p_0 \exp\left(-\dfrac{\operatorname{tr}\boldsymbol{\varepsilon}^{\mathrm{e}}}{\kappa}\right) + \beta\, d\left(\operatorname{tr}(\boldsymbol{\varepsilon}^{\mathrm{e}}_{\mathrm{D}})^2\right)^l & \text{for} \quad \operatorname{tr}\boldsymbol{\varepsilon}^{\mathrm{e}} > 0\,, \\ \alpha\, d\left(-\operatorname{tr}\boldsymbol{\varepsilon}^{\mathrm{e}} + \varepsilon_0\right)^n + \beta\, d\left(\operatorname{tr}(\boldsymbol{\varepsilon}^{\mathrm{e}})^2\right)^l & \text{for} \quad \operatorname{tr}\boldsymbol{\varepsilon}^{\mathrm{e}} \leq 0\,, \end{cases} \tag{1}$$

where $\boldsymbol{\varepsilon}^{\mathrm{e}}_{\mathrm{D}}$ is the deviatoric elastic strain component, the exponents n and l are equal to $n = 3$ and $l = 3/2$ in order to have a linear dependence of the bulk and shear stiffness on the square root of the mean pressure (as typically observed in sands), ε_0 is a constitutive parameter representing a small reference strain (here assumed

equal to 0.000 03), the effects of which are analysed in the next subsection. In order to have C0, C1 and nearly C2 continuity of the free energy density function, we must choose $\kappa = \varepsilon_0/2$ and $p_0 = 3\alpha\, d\, \varepsilon_0^2$. Finally, in order to have an elastic stiffness inspired to the small strain stiffness of sands taking into account the empirical relationship proposed by Hardin & Richart [11], the constitutive parameters d, α and β are equal to

$$d = \left(3230\,\frac{(2.97-e)^2}{1+e}\right)^2 p_{\mathrm{ref}}\, f\,, \tag{2a}$$

$$\alpha = \frac{5\nu - 1}{6\sqrt{3}(1-2\nu)}\beta\,, \tag{2b}$$

$$\beta = \frac{2(1+\nu)}{3\sqrt{3}(1-2\nu)}\,, \tag{2c}$$

where ν is a constitutive parameter (here assumed equal to 0.4) having the role of Poisson's ratio, e is the (constant) void ratio (here assumed equal to 0.7), $p_{\mathrm{ref}} = 1\,\mathrm{kPa}$ is a reference pressure and f is a reduction factor (here assumed equal to 1). For $f = 1$ the elastic stiffness coincides with that proposed by Hardin & Richart [11] within the small strain framework.

2.1. Continuity issues for the new hyper-elasticity law

In order to investigate the continuity of the proposed free energy density function, to perform some parametric analyses, and to show the qualitative responses of the proposed model, it is useful to consider the volumetric strain $\varepsilon_{\mathrm{v}}^{\mathrm{e}} = \mathrm{tr}\,\boldsymbol{\varepsilon}^{\mathrm{e}}$, the deviatoric strain $\varepsilon_{\mathrm{s}}^{\mathrm{e}} = \sqrt{\mathrm{tr}(\boldsymbol{\varepsilon}_{\mathrm{D}}^{\mathrm{e}})^2}$, and to evaluate the mean stress $p = \mathrm{tr}\,\boldsymbol{\sigma}/3$ and the deviatoric stress $q = 3/2\sqrt{\mathrm{tr}\,\boldsymbol{\sigma}_{\mathrm{D}}^2}$. According to these strain variables, the free energy density function (1) can be rewritten as

$$\varphi(\varepsilon_{\mathrm{v}}^{\mathrm{e}}, \varepsilon_{\mathrm{s}}^{\mathrm{e}}) = \begin{cases} \kappa\, p_0 \exp\left(-\dfrac{\varepsilon_{\mathrm{v}}^{\mathrm{e}}}{\kappa}\right) + \beta\, d(\varepsilon_{\mathrm{s}}^{\mathrm{e}})^3 & \text{for} \quad \varepsilon_{\mathrm{v}}^{\mathrm{e}} > 0\,, \\ \alpha\, d\,(-\varepsilon_{\mathrm{v}}^{\mathrm{e}} + \varepsilon_0)^3 + \beta\, d\left(\dfrac{1}{3}(\varepsilon_{\mathrm{v}}^{\mathrm{e}})^2 + (\varepsilon_{\mathrm{s}}^{\mathrm{e}})^2\right)^{\frac{3}{2}} & \text{for} \quad \varepsilon_{\mathrm{v}}^{\mathrm{e}} \le 0\,. \end{cases} \tag{3}$$

The stress components can be obtained as follows

$$p = \frac{\partial \varphi}{\partial \varepsilon_{\mathrm{v}}^{\mathrm{e}}} = \begin{cases} -p_0 \exp\left(-\dfrac{\varepsilon_{\mathrm{v}}^{\mathrm{e}}}{\kappa}\right) & \text{for} \quad \varepsilon_{\mathrm{v}}^{\mathrm{e}} > 0\,, \\ -3\alpha\, d\,(-\varepsilon_{\mathrm{v}}^{\mathrm{e}} + \varepsilon_0)^2 + \beta\, d\left(\dfrac{1}{3}(\varepsilon_{\mathrm{v}}^{\mathrm{e}})^2 + (\varepsilon_{\mathrm{s}}^{\mathrm{e}})^2\right)^{\frac{1}{2}} \varepsilon_{\mathrm{v}}^{\mathrm{e}} & \text{for} \quad \varepsilon_{\mathrm{v}}^{\mathrm{e}} \le 0\,. \end{cases} \tag{4}$$

which is C0 continuous in $\varepsilon_{\mathrm{v}}^{\mathrm{e}} = 0$ because $p_0 = 3\alpha\, d\, \varepsilon_0^2$, whereas

$$q = \frac{\partial \varphi}{\partial \varepsilon_{\mathrm{s}}^{\mathrm{e}}} = \begin{cases} 3\beta\, d\,(\varepsilon_{\mathrm{s}}^{\mathrm{e}})^2 & \text{for} \quad \varepsilon_{\mathrm{v}}^{\mathrm{e}} > 0\,, \\ 3\beta\, d\left(\dfrac{1}{3}(\varepsilon_{\mathrm{v}}^{\mathrm{e}})^2 + (\varepsilon_{\mathrm{s}}^{\mathrm{e}})^2\right)^{\frac{1}{2}} \varepsilon_{\mathrm{s}}^{\mathrm{e}} & \text{for} \quad \varepsilon_{\mathrm{v}}^{\mathrm{e}} \le 0\,, \end{cases} \tag{5}$$

which is continuous in $\varepsilon_{\mathrm{v}}^{\mathrm{e}} = 0$.

The tangent bulk elastic stiffness is given by

$$\frac{\partial p}{\partial \varepsilon_{\mathrm{v}}^{\mathrm{e}}} = \begin{cases} \dfrac{p_0}{\kappa} \exp\left(-\dfrac{\varepsilon_{\mathrm{v}}^{\mathrm{e}}}{\kappa}\right) & \text{for} \quad \varepsilon_{\mathrm{v}}^{\mathrm{e}} > 0\,, \\ 6\alpha\, d\,(-\varepsilon_{\mathrm{v}}^{\mathrm{e}} + \varepsilon_0) + \dfrac{\beta\, d}{3}\left(\dfrac{1}{3}(\varepsilon_{\mathrm{v}}^{\mathrm{e}})^2 + (\varepsilon_{\mathrm{s}}^{\mathrm{e}})^2\right)^{-\frac{1}{2}} (\varepsilon_{\mathrm{v}}^{\mathrm{e}})^2 & \\ \qquad + \beta\, d\left(\dfrac{1}{3}(\varepsilon_{\mathrm{v}}^{\mathrm{e}})^2 + (\varepsilon_{\mathrm{s}}^{\mathrm{e}})^2\right)^{\frac{1}{2}} & \text{for} \quad \varepsilon_{\mathrm{v}}^{\mathrm{e}} \le 0\,. \end{cases} \tag{6}$$

Taking account that $\kappa = \varepsilon_0/2$, equation (6) is continuous in $\varepsilon_{\mathrm{v}}^{\mathrm{e}} = 0$ only if $\varepsilon_{\mathrm{s}}^{\mathrm{e}} = 0$, whereas this is only approximately true if $\varepsilon_{\mathrm{s}}^{\mathrm{e}}$ is negligible. This holds true if the yield surface passes close or through the axis origin and the strain increment is small (thus the elastic predictor lays close to the yield surface and $\varepsilon_{\mathrm{s}}^{\mathrm{e}} \approx 0$).

The elastic, out-of-diagonal tangent stiffness term is given by

$$\frac{\partial p}{\partial \varepsilon_{\mathrm{s}}^{\mathrm{e}}} = \begin{cases} 0 & \text{for} \quad \varepsilon_{\mathrm{v}}^{\mathrm{e}} > 0\,, \\ \beta\, d\left(\dfrac{1}{3}(\varepsilon_{\mathrm{v}}^{\mathrm{e}})^2 + (\varepsilon_{\mathrm{s}}^{\mathrm{e}})^2\right)^{-\frac{1}{2}} \varepsilon_{\mathrm{v}}^{\mathrm{e}}\, \varepsilon_{\mathrm{s}}^{\mathrm{e}} & \text{for} \quad \varepsilon_{\mathrm{v}}^{\mathrm{e}} \le 0\,, \end{cases} \tag{7}$$

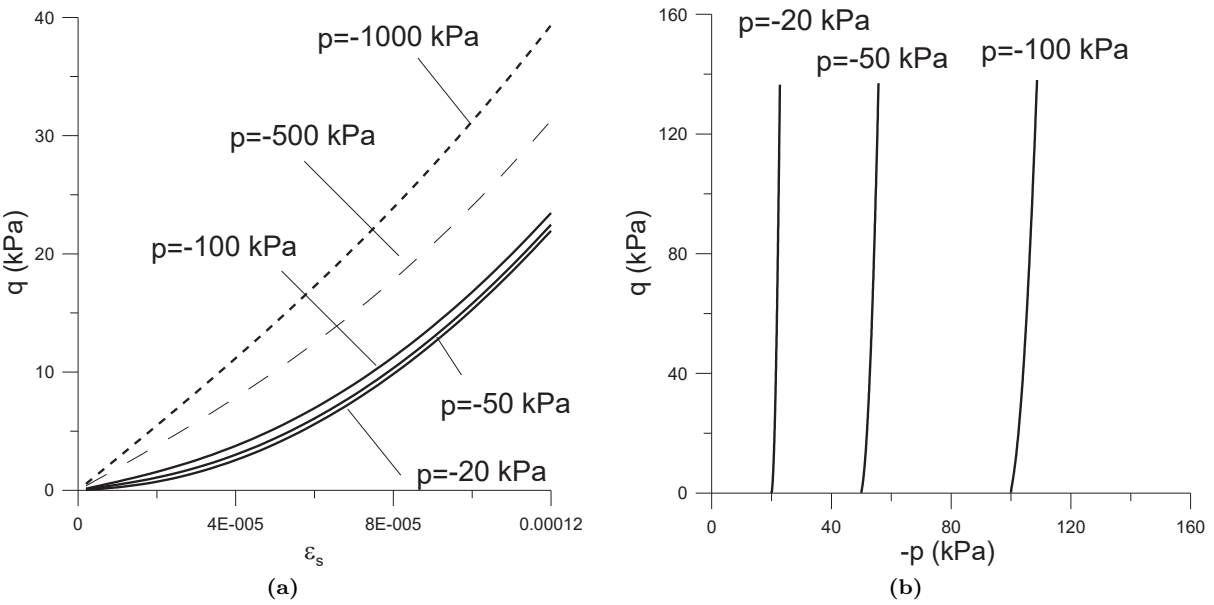

Figure 1: Typical elasticity model responses under different loading paths performed at constant $\varepsilon_{\mathrm{v}}^{\mathrm{e}}$ (corresponding to initial values of p equal to $-20\,\mathrm{kPa}$, $-50\,\mathrm{kPa}$, $-100\,\mathrm{kPa}$), $-500\,\mathrm{kPa}$, and $-1000\,\mathrm{kPa}$ and increasing $\varepsilon_{\mathrm{s}}^{\mathrm{e}}$.

which is continuous in $\varepsilon_{\mathrm{v}}^{\mathrm{e}} = 0$.

Finally, the tangent shear elastic stiffness is given by

$$\frac{\partial q}{\partial \varepsilon_{\mathrm{s}}^{\mathrm{e}}} = \begin{cases} 6\beta\, d\, \varepsilon_{\mathrm{s}}^{\mathrm{e}} & \text{for} \quad \varepsilon_{\mathrm{v}}^{\mathrm{e}} > 0\,, \\ 3\beta\, d \left(\frac{1}{3}(\varepsilon_{\mathrm{v}}^{\mathrm{e}})^2 + (\varepsilon_{\mathrm{s}}^{\mathrm{e}})^2 \right)^{-\frac{1}{2}} (\varepsilon_{\mathrm{s}}^{\mathrm{e}})^2 + 3\beta\, d \left(\frac{1}{3}(\varepsilon_{\mathrm{v}}^{\mathrm{e}})^2 + (\varepsilon_{\mathrm{s}}^{\mathrm{e}})^2 \right)^{\frac{1}{2}} & \text{for} \quad \varepsilon_{\mathrm{v}}^{\mathrm{e}} \leq 0\,. \end{cases} \tag{8}$$

which is continuous in $\varepsilon_{\mathrm{v}}^{\mathrm{e}} = 0$.

2.2. Typical simulations of hyper-elastic law

Figure 1 shows the typical model response for loading paths in which $\varepsilon_{\mathrm{s}}^{\mathrm{e}}$ increases, whereas $\varepsilon_{\mathrm{v}}^{\mathrm{e}}$ is kept constant at different values of p corresponding to $-20\,\mathrm{kPa}$, $-50\,\mathrm{kPa}$, $-100\,\mathrm{kPa}$, $-500\,\mathrm{kPa}$, and $-1000\,\mathrm{kPa}$. It can be observed that at small values of $\varepsilon_{\mathrm{s}}^{\mathrm{e}}$, the stiffness is higher at the larger values of p. In this case, the increase of initial shear stiffness (at small values of $\varepsilon_{\mathrm{s}}^{\mathrm{e}}$) is approximately proportional with the square root of mean pressure: at $p = -20\,\mathrm{kPa}$ the tangent shear stiffness is about $13.9\,\mathrm{MPa}$, at $p = -1000\,\mathrm{kPa}$ the tangent shear stiffness is about $91.8\,\mathrm{MPa}$, corresponding to a ratio of about 6.6, which is slightly smaller than the square root of the ratio of mean pressures, equal to 7.1. The overall deviatoric model response is however affected by the deviatoric strain $\varepsilon_{\mathrm{s}}^{\mathrm{e}}$ in Figure 1a, thus the response becomes stiffer and stiffer with the increase of the deviatoric stress. Anyway, as it can be observed in Figure 1b, the coupling between shear and volumetric response is weak, thus the loading path at constant $\varepsilon_{\mathrm{v}}^{\mathrm{e}}$, in a q–p space is nearly vertical, as in an isotropic elasticity.

Figure 2 shows the typical model response for loading paths in which $\varepsilon_{\mathrm{v}}^{\mathrm{e}}$ increases (in Figure 2a) or decreases (in Figure 2b) while keeping $\varepsilon_{\mathrm{s}}^{\mathrm{e}} = 0$. It can be noticed that the stress-strain response is smooth and the null value of mean stress is reached asymptotically at very large volumetric extensions.

Furthermore, Figure 2 shows the effects induced by the constitutive parameter ε_0. For negative values of volumetric strain (Figure 2b), the smaller is ε_0, the closer is the response to the original model of Gajo & Bigoni [5], corresponding to $\varepsilon_0 = 0$. On the other hand, for positive volumetric strains (Figure 2a), the smaller is ε_0, the sharper is the response of the model.

3. The continuous yield surface and the numerical implementation

In order to investigate the capabilities of the proposed hyper-elastic formulation in the context of practical engineering applications, a complete constitutive model including the yield surface should be implemented. To this purpose, the proposed hyper-elastic formulation is implemented as a user defined subroutine (UMAT) for Abaqus Unified FEA (Dassault Systèmes®) together with the C2 continuous approximation of the Mohr-Coulomb yield surface proposed by Abbo et al. [1], which is chosen because of its simplicity. However, we are convinced that similar results could have been obtained with different continuous approximations proposed in the literature [36, 22, 27, 23, 14].

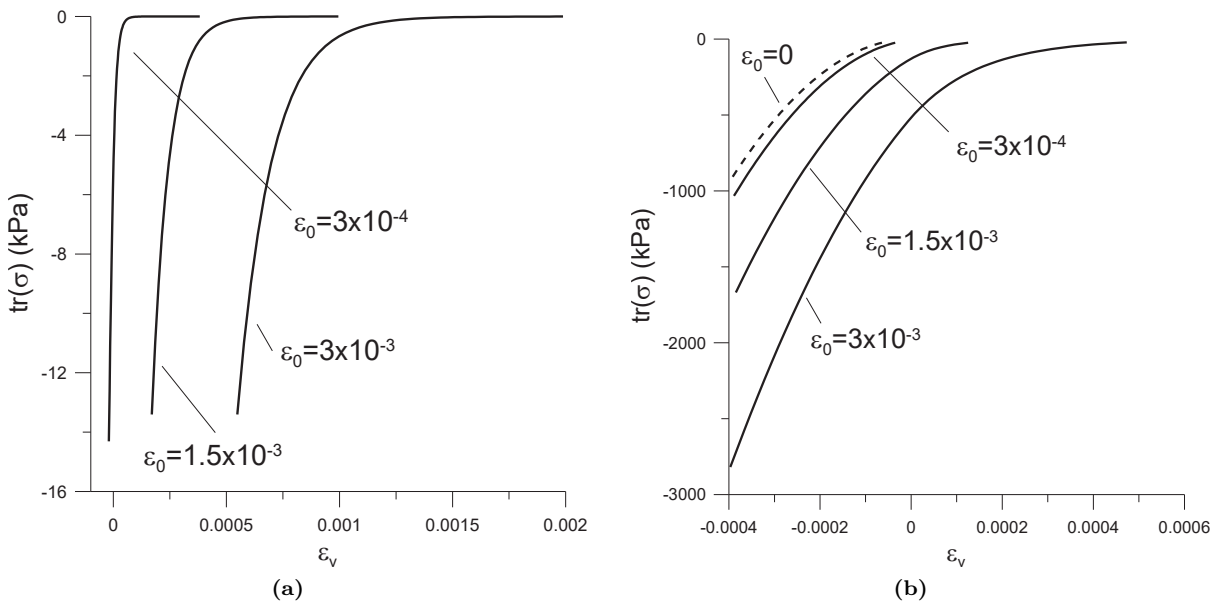

Figure 2: Elasticity model responses under loading paths at constant $\varepsilon_{\mathrm{s}}^{\mathrm{e}} = 0$ and increasing or decreasing $\varepsilon_{\mathrm{v}}^{\mathrm{e}}$, for different values of ε_0.

The C2 continuous approximation of the Mohr-Coulomb yield surface proposed by Abbo et al. [1] is here briefly recalled for the sake of completeness. The interested reader is referred to the original manuscript by Abbo et al. [1] for a more detailed description of the yield surface.

In the meridional plane, the sharp vertex at the apex of the yield surface is rounded according to the following hyperbolic approximation proposed by Abbo & Sloan [2]

$$F = \frac{\operatorname{tr}\boldsymbol{\sigma}}{3} + \sqrt{\operatorname{tr}\boldsymbol{\sigma}_{\mathrm{D}}^2\, K^2(\theta) + a^2 \sin^2\phi} - c\cos\phi = 0\,, \tag{9}$$

where c and ϕ are the constitutive parameters defining the cohesion and the friction angle, θ is the Lode angle, a is a constitutive parameter (see Figure 2 by Abbo et al. [1]) and $K(\theta)$ represents the following rounded deviatoric section of the yield surface

$$K(\theta) = \begin{cases} A + B\sin(3\theta) + C\sin^2(3\theta) & \text{for} \quad |\theta| > \theta_{\mathrm{T}}\,, \\ \cos(3\theta) - \dfrac{1}{\sqrt{3}}\sin\phi\sin\theta & \text{for} \quad |\theta| \le \theta_{\mathrm{T}}\,, \end{cases} \tag{10}$$

where the coefficient A, B, and C are functions of ϕ and θ_{T}, which are reported in the Appendix. The parameter θ_{T} is the transition angle specifying how accurately the rounded surface represents the true Mohr–Coulomb yield surface (see Figure 3 by Abbo et al. [1]), with $\theta_{\mathrm{T}} \to 30°$ giving the most accurate approximation. Herein $\theta_{\mathrm{T}} = 28.6°$ and $a = 0.6\,\mathrm{Pa}$ are assumed.

An implicit backward Euler algorithm is employed for the numerical integration of the model. This leads to the solution of a non-linear system of 7 algebraic equations (6 of which defining the flow rule and 1 the yield surface) in 7 unknowns (the 6 components of the plastic strain and the plastic multiplier), that is solved with a Newton-Raphson scheme, with a line-search algorithm [24]. Substepping is introduced only in the cases of convergence difficulties at the level of Gauss-point integration.

4. Mesh effects and parametric analysis in the limit load evaluation

The problems related to pathological mesh dependence that are typically involved in shear band analysis are well known in the literature. In order to analyse mesh dependence, we consider the problem of the limit load of a centrally loaded, non-yielding, shallow foundation (described in Figure 3a), because this is usually considered as one of the toughest problems, from a numerical point of view. As a result, this Section investigates in detail the influence of mesh refinement on the computed limit loads and on the rupture mechanisms of shallow foundations.

We consider a plane strain problem, with a centrally loaded, very rigid foundation (thickness $H = 1\,\mathrm{m}$), which has width $B = 10\,\mathrm{m}$ and has no embedment (thus the foundation base coincides with ground surface). The load is assumed homogeneously distributed over the length $l_1 = 2\,\mathrm{m}$ in the central part of the foundation. Soil is assumed completely saturated, with water table coinciding with ground surface and hydrostatic conditions, thus all computations are performed with the immersed unit weight of soil $\gamma' = 10\,\mathrm{kN\,m^{-3}}$. Soil strength is

defined by the friction angle $\phi = 35°$ and by the cohesion $c = 1\,\text{Pa}$, which corresponds to a low value. The flow rule is assumed associated, thus dilatancy ψ coincides with the friction angle ($\psi = \phi$). The contact friction at soil-foundation interface is considered equal to the soil friction angle. Soil stiffness is considered to coincide with the small-strain soil stiffness (and is accordingly, continuously updated during the loading process), whereas axial and bending compliances are assumed negligible. The effects of beam and soil stiffness are investigated in the next section.

Different types of meshes based on elements with quadratic formulation are investigated. In particular, this Section focuses on the effects of quadrangular meshes with different degrees of refinement and aspect ratio b/h (ranging between 1:4 to 4:1, Figure 3) and of triangular meshes (either structured or non-structured) with different degrees of refinement (Figure 4).

The foundation beam is discretised with 0.50 m beam elements with quadratic formulation. The soil meshes are considered to be either aligned (i.e. Figures 3b-3g) or not aligned with the mesh representing the foundation beam (as illustrated in Figures 3h and 3i). The soil domain width is equal to 450 m and its depth is equal to 250 m, corresponding to a wide domain where boundary effects are negligible also for the largest friction angles.

The boundary conditions of the soil domain are the following: no horizontal movement is permitted on the lateral sides, whereas the vertical displacements are constrained at the bottom. A load-controlled approach is used to explore the capabilities of the proposed constitutive model when applied to practical problems in which load-controlled conditions are needed, such as with yielding foundations or foundations subjected to an increasing load with constant eccentricity or load inclination.

4.1. Comparison between FEM and other numerical techniques

FEM results obtained from Abaqus (employing the proposed elasticity model) are compared with the upper bound computational limit analysis (CLA) method called Discontinuity Layout Optimization (DLO) (Smith & Gilbert [30]), with the lower bound solution proposed by Smith [29], and with the results of the characteristic lines method implemented in the ABC program written by Martin [17, 18, 19, 20]. The DLO procedure directly determines the limit load using optimization techniques to identify the critical collapse mechanism. The footing is modelled as a one dimensional element with a very large resistance to bending moments. The DLO procedure discretises the domain into a grid of nodes and the critical collapse mechanism is evaluated from a discrete set of slip-lines obtained by linking any pair of nodes. The accuracy of the DLO result is therefore a function of the nodal density employed. The domain size is calibrated in order to include the whole failure mechanism without affecting its shape. In general, for every value of friction angle, a nodal spacing refinement is performed below the foundation and along the borders of the soil domain (according to the software manual) with values ranging from $B/20$ to $B/80$, where B is the foundation width, which is equal to 10 m. For the largest value of internal friction angle, the nodal density approaches a target number of approximately 20 000 and several iterations are allowed.

The limit loads computed with FEM employing the meshes shown in Figures 3-4 are summarised in Table 1, whereas the corresponding load-displacement curves are shown in Figure 5. Some rupture mechanisms are shown in Figure 6.

The first observation that can be deduced from Figure 5 is that in all cases the load-displacement curves reaches a constant value (i.e. a plateau) at large displacements, denoting that a well established rupture mechanism has been obtained. This is considered fundamental for the evaluation of the limit load, because the simple lack of convergence is not sufficient to ensure the existence of a fully developed rupture mechanism. The second observation is that quadrangular meshes lead to limit loads laying within a very narrow range ($q_{\text{lim}} = 1781\,\text{kPa} \div 1820\,\text{kPa}$). From Table 2, it is interesting to observe that the limit loads computed with quadrangular elements fall between the upper bound load computed with DLO method ($q_{\text{lim}} = 1827\,\text{kPa}$) and the limit load computed with the characteristic lines method, using the ABC code ($q_{\text{lim}} = 1724\,\text{kPa}$), and the lower bound solution [29]. The effect of mesh refinement in FEM simulations is that the computed limit load decreases with the decrease of the mesh size, thus approaching the lower bound solution. It can be observed that shear bands become thinner with the decrease of mesh size, without affecting the rupture mechanism.

The narrow range of limit loads computed with the rectangular meshes is consistent with the rupture mechanisms shown in Figure 6. Similarly, the coarse triangular unstructured mesh leads to a slightly larger limit load ($q_{\text{lim}} = 1843\,\text{kPa}$), whereas the refined unstructured triangular mesh provides a smaller limit load ($q_{\text{lim}} = 1782\,\text{kPa}$), which is very close to the lower bound solution. In contrast, the structured triangular meshes lead to very dispersed values of the limit load ($q_{\text{lim}} = 1672\,\text{kPa} \div 1849\,\text{kPa}$). This confirms that obtaining a plateau in the load-displacement curves is not sufficient to ensure a reliable evaluation of the limit load. In fact, the rupture mechanisms shown in Figure 6 are non symmetric and thus do not correspond to the correct failure mechanism. The non symmetric rupture mechanism is induced by the non symmetry of the structured triangular mesh.

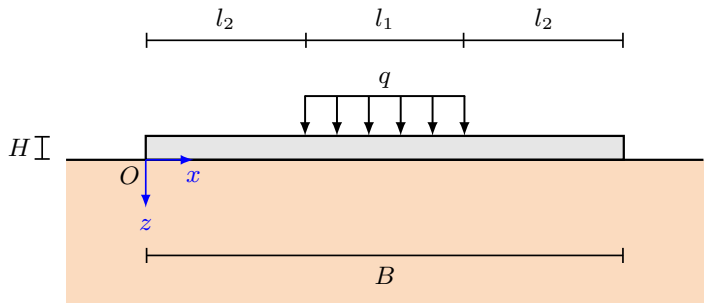

(a) *Reference scheme for the shallow foundation.*

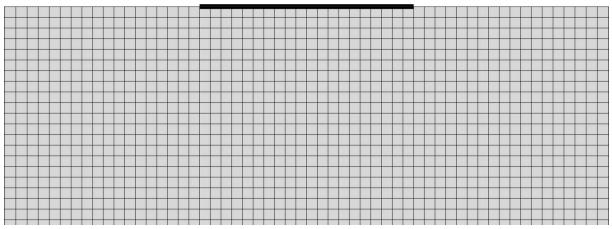

(b) *Coarse mesh.*

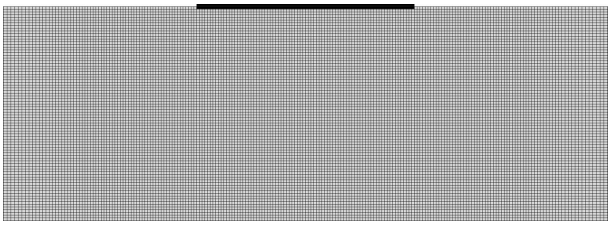

(c) *Refined mesh.*

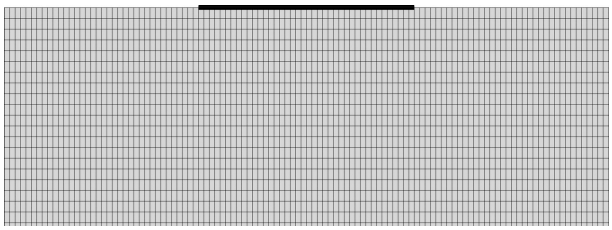

(d) *1:2 aspect ratio (b/h).*

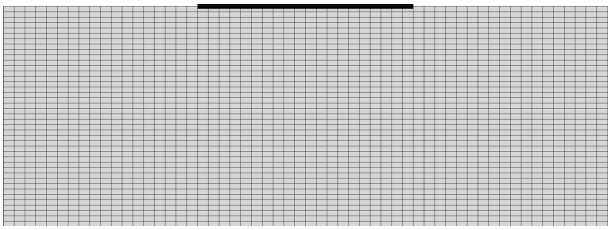

(e) *2:1 aspect ratio (b/h).*

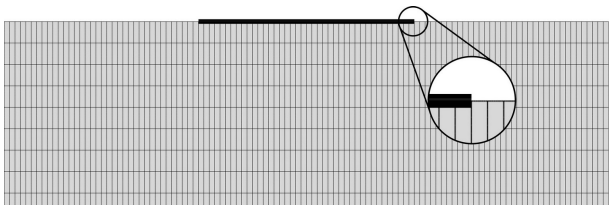

(f) *1:4 aspect ratio (b/h).*

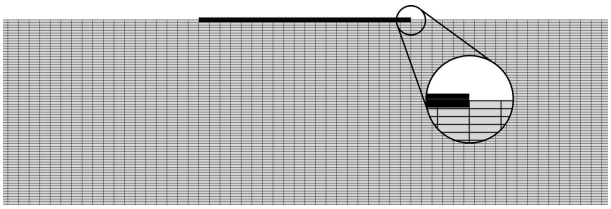

(g) *4:1 aspect ratio (b/h).*

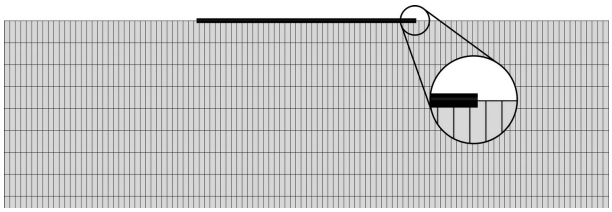

(h) *1:4 aspect ratio (b/h), foundation nodes not aligned with those of the soil.*

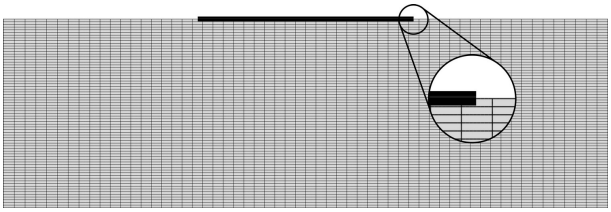

(i) *4:1 aspect ratio (b/h), foundation nodes not aligned with those of the soil.*

Figure 3: Comparison of the quadrangular meshes employed for the shallow foundation problem, solved with the proposed model implemented in Abaqus. In figures (b)-(i) the foundation beam is represented with a black solid line with arbitrary thickness for illustrative purpose only (there is no penetration between the foundation beam and the soil). The inset highlights the alignment (figures (f) and (g)) and the misalignment (figures (h) and (i)) between the foundation and the soil meshes.

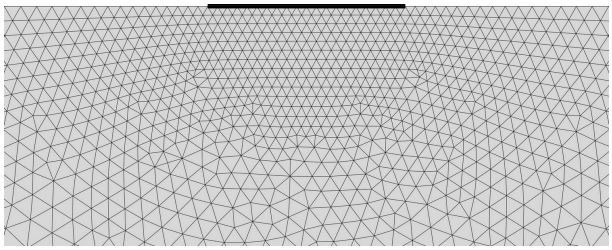

(a) *Free mesh refined in the neighbourhood of the foundation.*

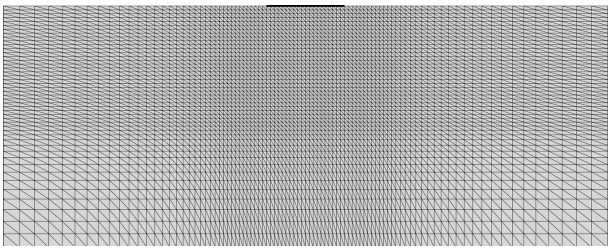

(b) *Structured mesh refined in the neighbourhood of the foundation.*

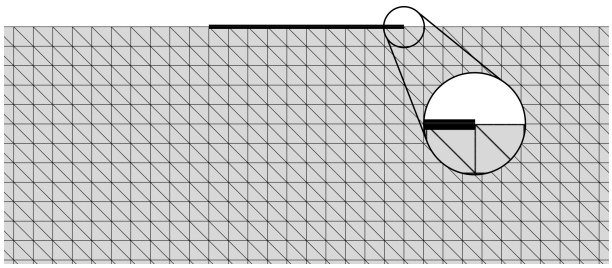

(c) *Structured mesh.*

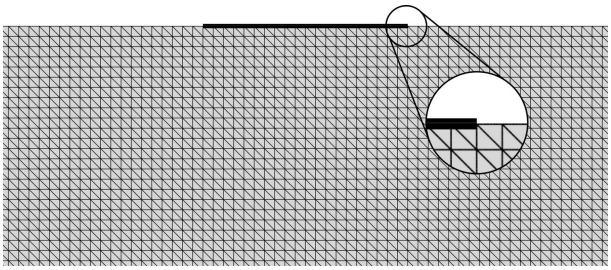

(d) *Refined structured mesh.*

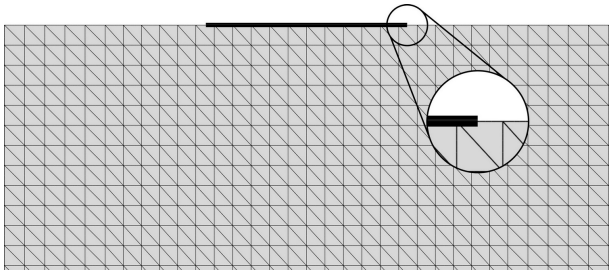

(e) *Structured mesh, foundation nodes not aligned with those of the soil.*

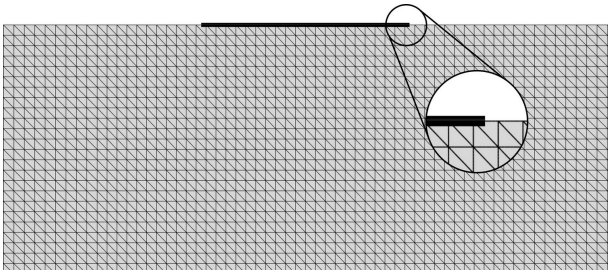

(f) *Refined structured mesh, foundation nodes not aligned with those of the soil.*

Figure 4: Comparison of the triangular meshes employed for the shallow foundation problem, solved with the proposed model implemented in Abaqus. In figures (a)-(f) the foundation beam is represented with a black solid line with arbitrary thickness for illustrative purpose only (there is no penetration between the foundation beam and the soil). The inset highlights the alignment (figures (c) and (d)) and the misalignment (figures (e) and (f)) between the foundation and the soil meshes.

Table 1: Mesh performance comparison in terms of limit load evaluation (for a non-yielding foundation under a centred load) for the case of $\phi = 35°$. Mesh size of the foundation is equal to 0.5 m in all of the models.

Label	Element shape	Nr. of elements	Element distribution	Alignment with foundation mesh	Aspect ratio b/h	Minimun size	q_{lim}
(A)	Quad	15 620	Biased	Yes	1	0.5 m	1809.7 kPa
(B)	Quad	39 400	Biased	Yes	1:2	0.125 m	1742.8 kPa
(C)	Quad	117 740	Biased	Yes	1	0.125 m	1740.1 kPa
(D)	Quad	33 900	Homogeneous	Yes	2:1	0.25 m	1805.7 kPa
(E)	Quad	55 800	Homogeneous	Yes	4:1	0.125 m	1775.9 kPa
(F)	Quad	56 172	Homogeneous	No	4:1	0.125 m	1781.0 kPa
(G)	Quad	42 600	Homogeneous	Yes	1:2	0.25 m	1761.2 kPa
(H)	Quad	27 600	Homogeneous	Yes	1:4	0.25 m	1768.3 kPa
(I)	Quad	27 692	Homogeneous	No	1:4	0.25 m	1798.7 kPa
(J)	Tri	4806	Free, biased	Yes	1	0.5 m	1831.9 kPa
(K)	Tri	11 790	Free, biased	Yes	1	0.25 m	1781.5 kPa
(L)	Tri	12 992	Structured, biased	Yes	1	0.5 m	1833.3 kPa
(M)	Tri	12 000	Structured, homogeneous	Yes	1	1.0 m	1936.4 kPa
(N)	Tri	12 160	Structured, homogeneous	No	1	1.0 m	1634.5 kPa
(O)	Tri	42 600	Structured, homogeneous	Yes	1	0.5 m	1830.9 kPa
(P)	Tri	42 884	Structured, homogeneous	No	1	0.5 m	1671.1 kPa

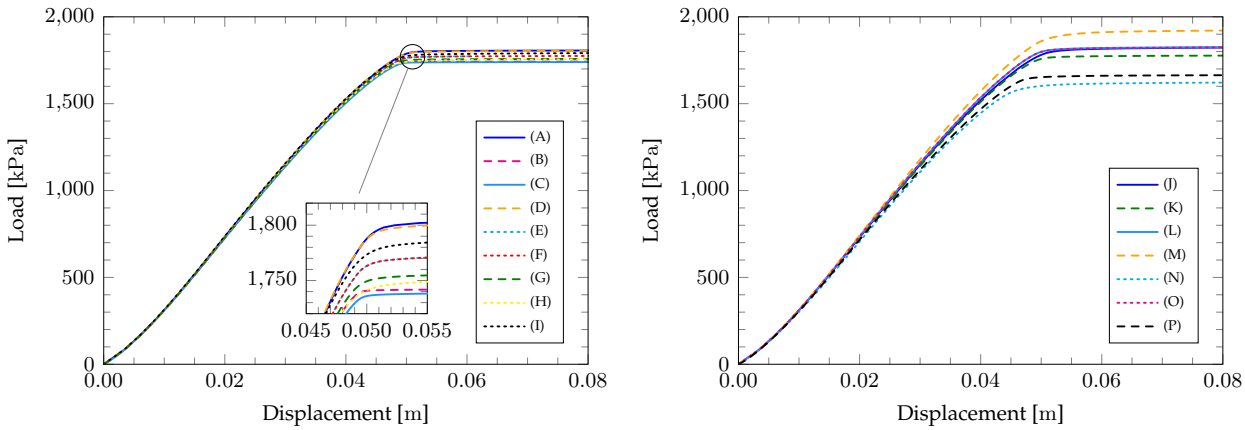

(a) *Quadrangular mesh.* **(b)** *Triangular mesh.*

Figure 5: Load-displacement curves for the centrally loaded foundation. A comparison is made between different meshes for the same internal friction angle, equal to 35°. The plateau exhibited by the structured triangular mesh denotes a limit load but does not correspond to the correct failure mechanism, whereas the free triangular mesh is symmetric and leads to a correct failure mechanism.

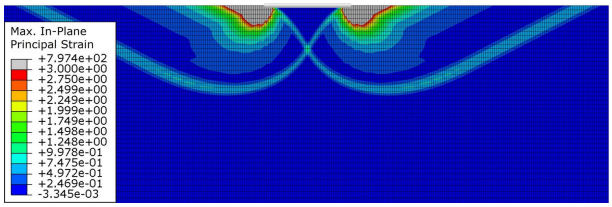

(a) *Quadrangular mesh with aspect ratio (b/h) equal to 1:2.*

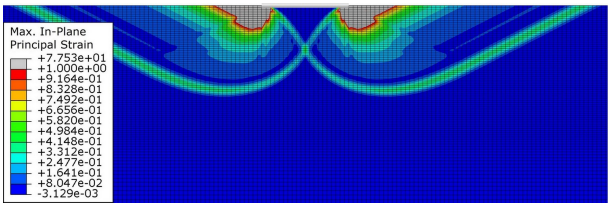

(b) *Quadrangular mesh with aspect ratio (b/h) equal to 2:1.*

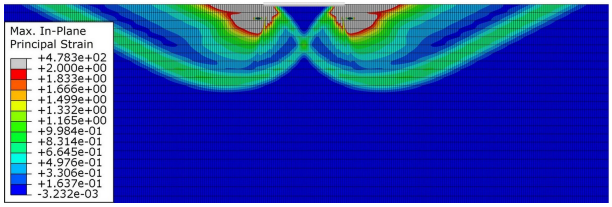

(c) *Quadrangular mesh with aspect ratio (b/h) equal to 1:4.*

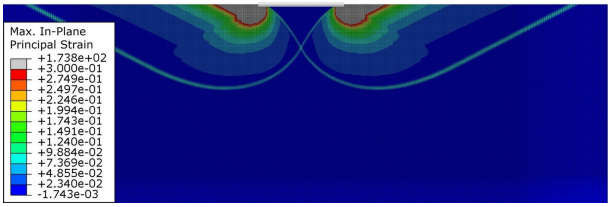

(d) *Refined quadrangular mesh with further refinement beneath the foundation.*

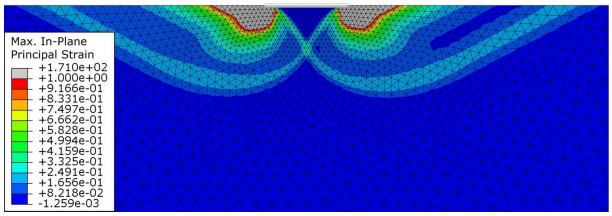

(e) *Free triangular mesh refined beneath the foundation.*

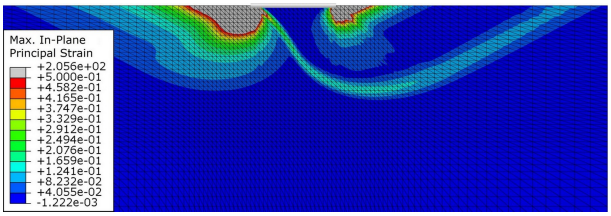

(f) *Structured triangular mesh refined beneath the foundation.*

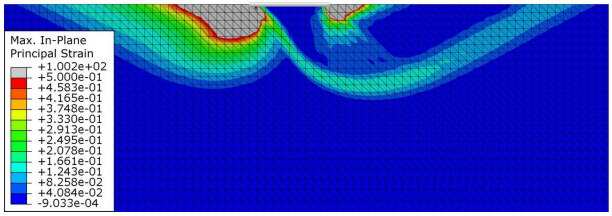

(g) *Coarse structured triangular mesh.*

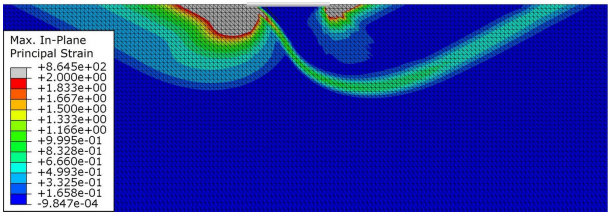

(h) *Refined structured triangular mesh.*

Figure 6: Comparison of the failure mechanism for different types of quadrangular and triangular mesh for a soil with internal friction angle equal to 35° (the strain field is shown). The lack of symmetry of the mesh, which may occur in the case of a structured or free triangular mesh, leads to a wrong failure mechanism, showing a non-symmetric behaviour, which is not correct.

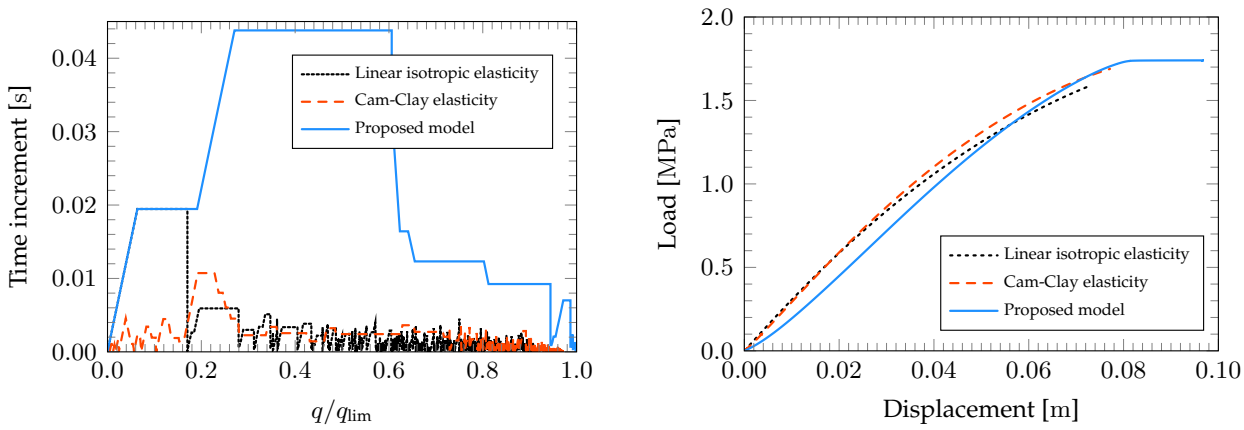

(a) *Comparison of the time increments chosen by the program during the analysis.*

(b) *Comparison of the load-displacement curves.*

Figure 7: Comparison of the performance for different types of elasticity laws using the mesh depicted in Figure 3c.

4.2. Comparison with other elasticity laws

The case study described above can also be analysed with other elasticity laws, in order to compare the convergence rates and accuracies of different elasticity models. To this purpose, the linear elastic isotropic elasticity law and the Cam-Clay elasticity law have been considered. These two formulations have been implemented as user defined subroutines (UMAT) for Abaqus Unified FEA (Dassault Systèmes®) together with the C2 continuous approximation of the Mohr-Coulomb yield surface as described in Section 3. It is important to remark that, the same implementation technique is employed for all elasticity models, thus the external routine is written exactly in the same way, and the line-search algorithm and the substepping technique are exactly the same; therefore, the only difference among the elasticity models is the expression of the elastic potential. The same friction angle (35°), the same value of cohesion (1 Pa), and same mesh have been used for all elasticity models. The elastic constants of the linear isotropic elasticity model and of the Cam-Clay elasticity model have been chosen in order to obtain approximately the same load-displacement response that is obtained with the proposed elasticity model (see the results of Table 1 and Figure 5a). In order to compare the convergence rates, the same time stepping settings have been used in all models. In particular, the maximum time increment is assumed very large (corresponding to 10% of the limit load) so that the optimal time stepping is automatically selected by Abaqus algorithm depending on the convergence rate of the equilibrium iterations.

Three types of quadrangular meshes (labelled as (A), (B), and (C) in Table 1) have been considered. For the sake of conciseness, only the results obtained using the refined quadrangular mesh (C), depicted in Figure 3c, are reported in detail in this Section.

In Figure 7a, the linear isotropic elasticity model exhibits large time increments only at a small applied loads (roughly smaller than 45% of the limit load) and soon after the time increments are strongly reduced. The Cam-Clay elasticity model exhibits relatively small time increments from the very beginning of the analysis but, in contrast with the linear isotropic elasticity model, does not show such frequent strong reductions, at least until approximately 75% of the limit load is reached. The proposed elasticity model shows less convergence problems as compared with the other elasticity models, so that the time increments are automatically increased up to values that are significantly larger than those used for the linear isotropic elasticity and the Cam-Clay elasticity models. As approximately 60% of the limit load is reached, the time increment for the proposed model is strongly reduced but it still remains by far larger than that of the other elasticity models. It is worth noting that a strong reduction of the time increments for the proposed elasticity model is needed close to the limit load when the horizontal plateau of the load-displacement curve is reached (as illustrated in Figure 7b). This is consistent with the load-control of these simulations. Each simulation is terminated when convergence is not achieved.

Although the linear isotropic elasticity and the Cam-Clay elasticity models use smaller time increments, the number of severe discontinuities, cutbacks, and attempts made by the solution algorithm are significantly larger than those needed for the proposed elasticity model. This is why it is useful to compare also the different elasticity models in terms of computing time. To this aim, in the simulations reported in Figure 7, if the proposed elasticity model is assumed to be the reference model with a computing time equal to 1, the normalised computing times for the linear isotropic elasticity model and for the Cam-Clay elasticity model turn out to be equal to 2.54 and to 5.75, respectively. Thus the proposed elasticity model is much faster than the others, notwithstanding the fact that it is able to reach a well defined plateau at much larger settlements than the other models.

Figure 7b clearly shows that, when using the same mesh, time stepping options, and material properties, only the proposed elasticity model can reach the limit load and a well defined rupture mechanism, whereas the other elasticity models present a lack of convergence before the limit load is approached. In particular, the linear isotropic elasticity model and the Cam-Clay elasticity model reach up to the 91% and the 97% of the limit load respectively, values that are not large enough to determine the plateau of the load-displacement curve, and therefore the limit load and the rupture mechanism. In addition, the linear isotropic elasticity model and the Cam-Clay elasticity model have an unpredictable behaviour in terms of performance: a very small change in the choice of material parameters or mesh refinement can lead to a wide range of scenarios, ranging from simulations that may stop soon after the application of a very small load (i.e. less than 10% of the limit load) to simulations that can run until the applied load is very close to the limit load (in any case without reaching a well defined failure mechanism and the horizontal plateau of the load-displacement curve). In contrast, the capability of the proposed model to reach the limit load is not affected by the mesh refinement (provided that the mesh is symmetric, as discussed in Section 4.1) or by the choice of elastic properties. As a result, the proposed model has a much more robust behaviour than the other elasticity models and allows to reach the fully developed rupture mechanism, in contrast with the other models. It is worth adding that the elasticity model proposed by Houlsby et al. [12] has been also considered, but it was not included in the previous comparisons because its numerical performance was much worse than that of the elasticity models considered here.

5. Numerical evaluations of the limit load

This Section investigates the capabilities of the proposed FEM approach in evaluating the limit load of centrally loaded, non yielding, shallow foundations for different values of the friction angle, and the limit load of trap doors. These two examples have been selected taking into account of their numerical challenges and their engineering relevance and therefore can be exploited as a valuable benchmark for the proposed hyper-elastic formulation.

5.1. The limit load of a centrally loaded, non yielding, shallow foundation

At first glance, the evaluation of the limit load of a centrally loaded, shallow foundation may appear as a useless numerical exercise, because upper and lower bound solutions and the solution based on characteristic lines method are currently available. However, many problems related to the limit load of shallow foundations remain still open. In particular, Gajo & Smith [8] have recently investigated the possible formation of combined rupture mechanisms in the soil and in the foundation assuming undrained conditions, leading to an important reduction of the limit load for shallow foundations. However, the problems of the drained conditions remains still unexplored and can be tackled only by using numerical methods, either based on FEM (such as the one proposed here) or on the application of the upper bound limit analysis (such as DLO). In contrast with the the upper bound limit analysis, FEM method has the advantage of studying regions where yielding is not reached, such as the upper structure, that can be loaded in the elastic regime. On the other hand, all the computations described in this Section are performed with two numerical methods (FEM with the proposed constitutive model and DLO) in order to validate the proposed constitutive model.

It is worth remarking that the analysis of a shallow foundation with null embedment is very important in engineering applications. In fact, although shallow foundations usually have a minimum embedment of $1\,\mathrm{m} \div 2\,\mathrm{m}$ according to technical standards, at the limit condition, due to load eccentricity or foundation yielding, foundation base may partially detach from soil, thus inducing locally a null embedment condition.

Table 2 provides the comparison between the limit loads evaluated with the upper bound method (DLO), with the lower bound method [29], with the characteristic lines method (ABC), and with FEM method (employing in the latter a load-controlled approach and two different levels of mesh refinement) for friction angles ϕ ranging between 15° and 45°. It can be observed that in all of these cases FEM solution lays approximately within the range of the upper bound and lower bound solutions. The rupture mechanisms obtained with FEM analyses are compared with those obtained from DLO and ABC, as illustrated in Figure 8. It can be noted that these failure mechanisms are perfectly superposed with each other for the various friction angles.

Figure 9 shows the regions in which the mobilized friction angle ϕ_m is equal to the soil friction angle ϕ (more precisely, the regions where $\phi_\mathrm{m} \in [\phi - 0.01°; \phi + 0.01°]$) and is thus at failure. It can be observed that the mobilized friction angle is equal to soil friction angle within the rupture mechanism highlighted by FEM analyses, characteristic lines method and upper bound solution (DLO); moreover there is a bulb of soil below the rupture mechanism where the soil is at rupture as well. This bulb becomes deeper with the increase of the friction angle. The extension of this bulb of soil at rupture depends on the earth pressure at rest, as shown in Figure 10 for 45°. For $K_0 = 5$ (namely for K_0 close to the coefficient of passive earth pressure), the amplitude of the bulb of soil at rupture is practically null. Poisson's ratio reveals to be ineffective on the shape and amplitude of the bulb of soil at rupture. The existence of the bulb of soil at rupture is fairly unexpected from the upper bound solution and from the solution based on characteristic lines method. However, it is worth noting that the

existence of this bulb from FEM analysis is not in contrast with the other solutions because the bulb cannot lead to a rupture mechanism (because it is completely confined by non yielding soil) and it is below the characteristic lines fan, thus it cannot be detected with the characteristic lines method.

The load-displacement curves obtained with a coarse and with a refined mesh are compared with each other in Figure 11, for friction angles ϕ ranging between 15° and 45°. It can be observed that in all cases, the increase of mesh refinements leads to a slight decrease of the computed limit load and to a sharper transition from elastic to plastic response. In addition, the mean slope of the 'elastic' portion of the loading curves increases with the increase of the limit load. The effects of earth pressure coefficient at rest (K_0) on the load-displacement curves is shown in Figure 12. It can be observed that, due to the dependence of elastic stiffness on stress state, a higher value of K_0 leads to a stiffer elastic response.

For the structural design of the shallow foundation at ultimate conditions it is important to know the distribution of bending moments and shear and axial forces along the foundation beam. For the sake of completeness, Figure 13a shows the distribution of contact pressure at limit conditions as resulting from FEM analyses for $\phi = 30°$ using two different levels of mesh refinement. It can be noted that the contact pressures are very sensitive to mesh refinement: in fact, spurious oscillations can be observed for the coarser mesh. In any case, the contact pressures have a sort of parabolic distribution that is much different with respect to the constant distribution obtained under undrained conditions (Gajo & Smith [8]). In particular, the low contact pressure at the lateral sides of the foundation implies the possibility of a partial slippage at soil-foundation interface. Figure 14 shows the distribution of relative displacements at soil-foundation contact for different soil friction angles and mesh refinement levels. It can be observed that the increase of soil friction angle leads to a decrease of the slippage region, that becomes very small at 45°, whereas the central part of the foundation is not affected by slippage. The distribution of tangential stresses at the foundation base shown in Figure 13b for $\phi = 30°$ using two different levels of mesh refinement is consistent with the distribution of the slippage shown in Figure 14. In particular, it can be observed that at the lateral sides of the foundation, the shear stress is limited by the shear strength in the portion of foundation where slippage occurs, whereas in the central part of the foundation, the shear stress decreases and becomes null at the centre of the foundation, thus it is certainly smaller than the shear strength. In this region, the contact shear stress depends on contact stiffness and the amount of relative displacements.

The results are presented also in terms of bending moments, shear force, and axial force in the foundation beam, that are shown in Figures 17, 16 and 15 for two different levels of mesh refinement. These internal actions are associated to the contact pressures and shear stresses at the foundation base. It can be observed that the distribution of bending moments is scarcely affected by the mesh refinement, in contrast with the distribution of axial forces. The comparison between FEM and DLO results in terms of bending moments and shear forces as shown in Figures 17 and 16 is excellent for all soil friction angles considered in this text. In contrast, the computed axial forces (Figure 15) need very high mesh refinement to be considered reliable. This is a direct result of the slippage at soil-foundation interface. Moreover, the agreement with DLO results is much worse in this case. In particular, DLO results are consistent with FEM evaluations only in the slippage regions, where the limit resistance is reached, but in the central static wedge the values are not reliable. These differences between DLO and FEM are however expected, where a full width static wedge forms (for a fully rough base), because in this area failure at the soil-foundation interface does not occur. As a result, the rigid-plastic formulation in DLO can give a range of possible distributions of internal actions, and in this case it generates a distribution of shear stresses in equilibrium with the applied load and closer to yield across the full width in comparison with FEM, which gives a generally lower non-yielding distribution of shear stresses based on elastic material and contact behaviour. In fact, in DLO analyses both soil and foundation are considered perfectly rigid up to the yield surface. In contrast, in the external regions of the foundation, where slippage occurs and the shear stress at soil-foundation contact reaches the rupture value, the consistency between FEM and DLO is excellent. No slippage occurs for $\phi \geq 45°$, thus the consistency of DLO with FEM is weak along the whole foundation beam.

The maximum values of the bending moments, shear force, and axial force in the foundation beam are summarised in the Table 2. Due to the shear stresses at the soil-foundation interface, very high tensile axial forces are induced in the foundation beam. It is worth remarking that in the typical engineering design practice, only the bending moment is considered, whereas the tensile axial forces are usually neglected. This has important consequences because foundation yielding (either in bending or in axial direction) may lead to combined rupture mechanisms both in soil and in the foundation leading to a large reduction of the limit load. This subject will be explored in a forthcoming paper.

Finally, Figure 18 shows a parametric analysis of the effects of beam and soil stiffness (with beam thickness h ranging between 0.5 m and 2 m and soil stiffness reduction parameter f ranging between 1 and 0.99) on the limit response. Within the limit analysis theory, it is well accepted that the limit conditions should not depend on the elastic properties of soil and of beam. In Figure 18 this holds true also for FEM analyses, as far as the limit load, the shear forces, and the bending moments are considered. In contrast, the axial force strongly depends on both soil and beam stiffnesses. Larger discrepancies can be observed where the regions of relative slippage at soil-foundations interface are smaller, corresponding to the cases of large friction angles. This is a further

Table 2: Comparison between the limit load evaluated with the proposed constitutive model, implemented in Abaqus, and the limit load evaluated with ABC and DLO for a non-yielding foundation under a centred load. Axial force, shear force, and bending moment per unit length in the foundation beam are evaluated in Abaqus.

ϕ	15°	20°	25°	30°	35°	40°	45°
q_{lim} [kPa] (Abaqus†)	63.60	151.60	345.38	779.44	1808.40	4509.20	12320.0
q_{lim} [kPa] (Abaqus*)	60.83	145.66	332.72	754.16	1754.40	4351.20	11776.0
q_{lim} [kPa] (ABC)	59.03	141.90	324.60	737.96	1723.69	4270.51	11632.4
q_{lim} [kPa] (DLO)	62.06	148.5	338.2	764.8	1827	4528	12500
N_γ (Abaqus†)	1.272	3.032	6.907	15.59	36.17	90.18	244.3
N_γ (Abaqus*)	1.216	2.913	6.654	15.08	35.09	87.02	235.5
N_γ (ABC)	1.181	2.838	6.492	14.76	34.37	85.41	232.6
N_γ (DLO)	1.241	2.970	6.764	15.30	36.54	90.56	250.0
N_{max} [MN m^{-1}] (Abaqus†)	0.0634	0.1815	0.4675	1.051	2.309	4.894	11.70
N_{max} [MN m^{-1}] (Abaqus*)	0.0569	0.1495	0.355	0.782	1.717	3.994	10.21
V_{max} [MN m^{-1}] (Abaqus†)	0.2069	0.5105	1.187	2.787	6.569	16.15	43.77
V_{max} [MN m^{-1}] (Abaqus*)	0.2023	0.4971	1.159	2.661	6.239	15.58	42.99
M_{max} [MN] (Abaqus†)	0.4196	1.056	2.541	6.049	14.66	37.28	102.3
M_{max} [MN] (Abaqus*)	0.3924	0.9824	2.352	5.538	13.26	33.71	94.08

† Coarse mesh, 0.5 m element size for the soil and for the foundation.
* Refined mesh, 0.2 m element size for the soil, 0.25 m element size for the foundation.

confirmation that at the highest friction angles, axial forces cannot be found only with considerations based on the limit equilibrium. Also the effects of parameter ν on the evaluation of the limit load are investigated; however, these effects are negligible, thus they are not reported for the sake of conciseness. It is worth adding that numerical convergence difficulties may arise with highly deformable beams on high friction soils (e.g. an unrealistic 0.5 m thick beam on a $\phi = 45°$ soil).

5.2. The active and passive trapdoor problem

Soil arching phenomena resulting from stress redistribution have been analysed using physical and analytical modelling of trapdoor systems [33, 13, 31, 21, 26]. In the active case, the downward movement of the trapdoor causes a reduction of soil stress immediately above the trapdoor and an increase of stress in the adjacent soil mass. The opposite trend occurs in the case of passive trapdoor. Both cases are useful for providing a clearer understanding of many engineering problems, such as ground anchors, soil pressures on tunnels, sinkholes, etc. Therefore, due to its importance, the trapdoor problem is investigated in order to further validate the performance of the proposed hyper-elastic model.

The main variables governing the trapdoor response are the soil properties and the ratio between the height of soil cover and the width of the trapdoor H/B. Finite element solutions of this problem were presented by Koutsabeloulis & Griffiths [13], who employed fifteen-node, triangular elements with 12 or 16 integration points. In all the analyses, a displacement-controlled approach is used. Most of their simulations were performed with a non-null cohesion intercept and in all results a non-associated flow rule is considered, with a null dilatation or an angle of dilatancy much smaller than the friction angle. Active and passive trapdoor problems were investigated also recently by other authors [4, 3, 34, 10, 9, 35, 15] by means of numerical and experimental models.

In the numerical tests discussed below, 8-node rectangular elements and a displacement-controlled approach are employed. The geometry of the problem is shown in Figure 19. Null friction is considered at all external boundaries. Mesh refinement is such that the smaller element size is equal to 0.25 m and aspect ratio $h/b = 1$. Soil cohesion and submerged unit weight are assumed equal to $c = 1$ Pa and $\gamma' = 10\,\text{kN m}^{-3}$.

FEM simulations are performed for different H/B ratios and the passive and active load ratio are evaluated for the case of $\phi = 35°$. In all of the FEM models, the soil domain is sufficiently large in order to avoid boundary effects. To this purpose, the following conditions are applied to the length L (see Figure 19): $L = 5B$ and $L > 2H$, with $B = 5.0$ m. Figure 20 shows the displacement and strain fields (highlighting the associated rupture mechanism) for the active and passive trapdoor problem, for friction angle equal to $\phi = 35°$, associated flow rule, and aspect ratio of the trapdoor equal to $H/B = 1.2$. Similar behaviour is obtained with the proposed model for other values of H/B, which can be deduced from Figure 21.

A comparison is made with the results obtained by Smith [28], which are summarised in Figure 21: the black solid and dashed lines correspond to the solutions obtained with DLO by Smith, whereas the blue and the orange curves correspond to the FEM results. It can be noted that FEM results are practically superposed to those obtained with DLO for the passive trapdoor problem until the H/B ratio is lower than 7, whereas

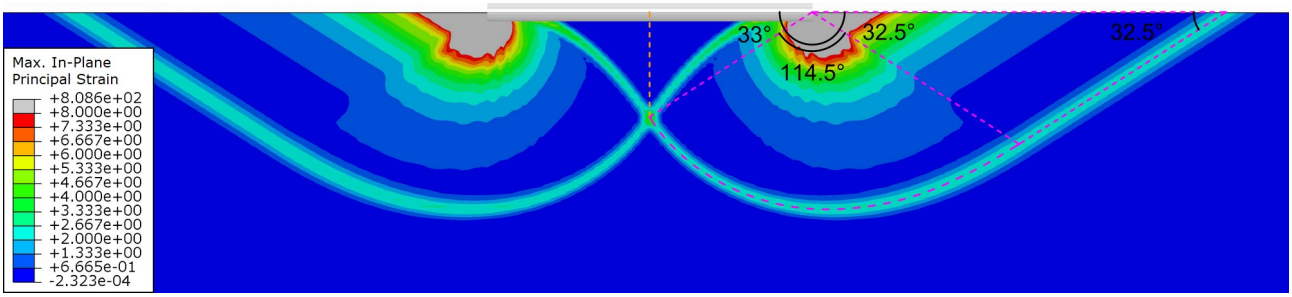

(a) $\phi = 25°$.

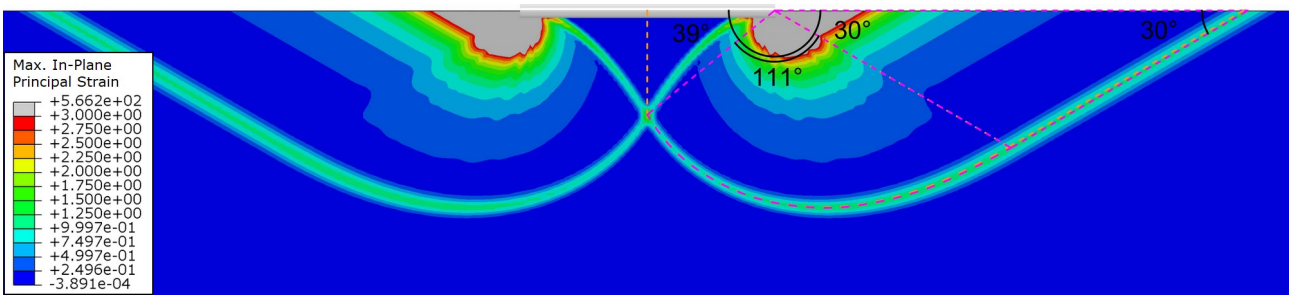

(b) $\phi = 30°$.

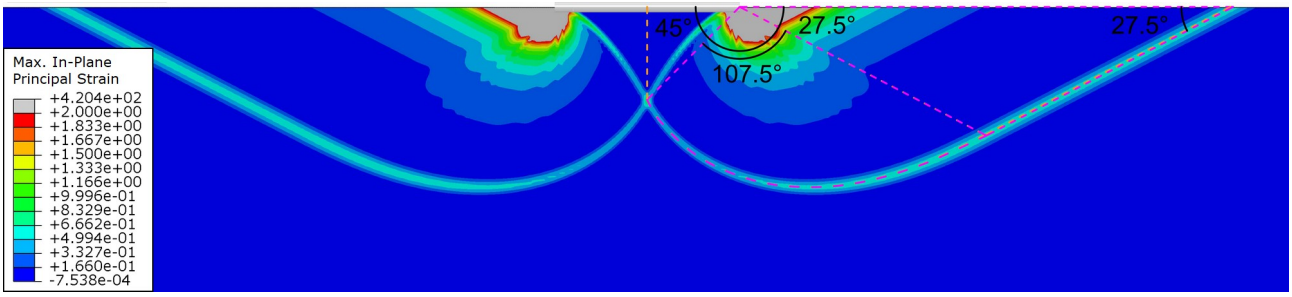

(c) $\phi = 35°$.

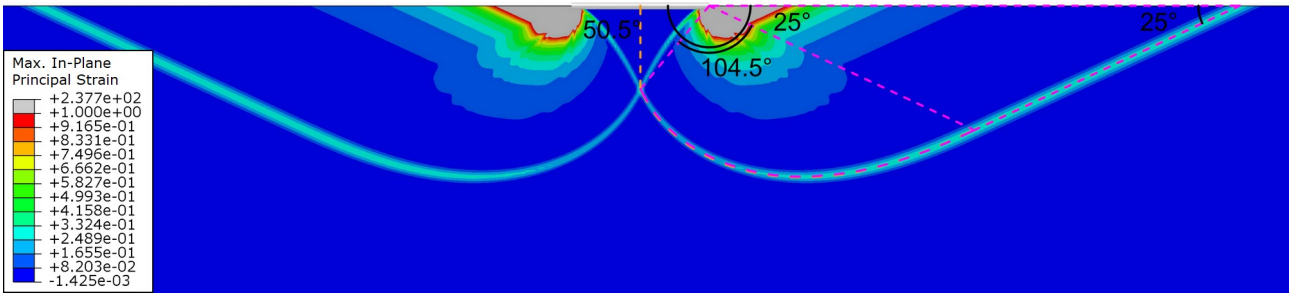

(d) $\phi = 40°$.

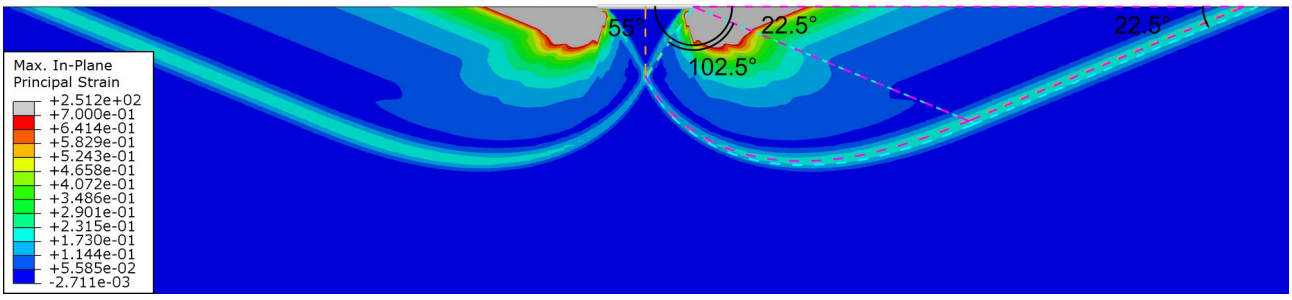

(e) $\phi = 45°$.

Figure 8: Comparison of the failure mechanisms obtained from the proposed model (implemented in Abaqus and shown magenta), from ABC (shown orange), and form DLO (shown cyan). The slip lines are practically overlapped in the first four cases (a)-(d), and a very minimal difference can be observed in the last case (e), where DLO solution shows a slightly bigger failure mechanism. This confirms that the failure mechanism obtained from three different techniques are almost the same.

(a) $\phi = 15°$.

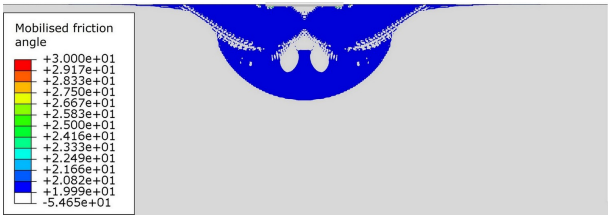

(b) $\phi = 20°$.

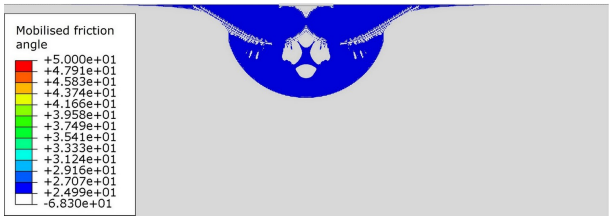

(c) $\phi = 25°$.

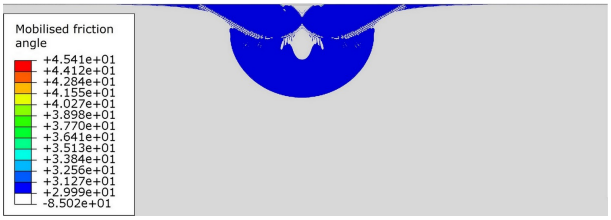

(d) $\phi = 30°$.

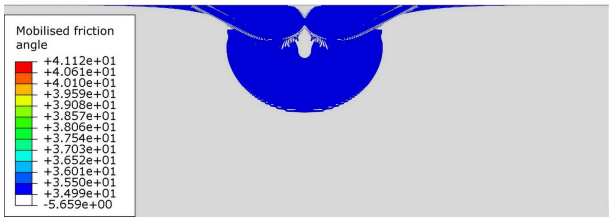

(e) $\phi = 35°$.

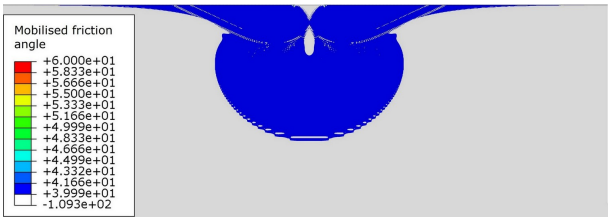

(f) $\phi = 40°$.

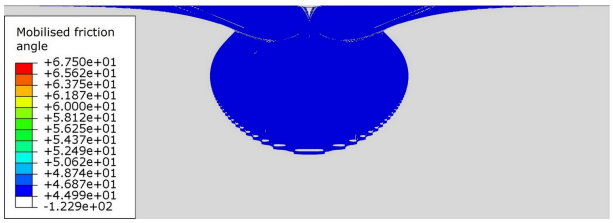

(g) $\phi = 45°$.

Figure 9: Comparison of the mobilised friction angle (expressed in degrees) for earth pressure at rest equal to $K_0 = 1$ and Poisson's ratio equal to 0.4.

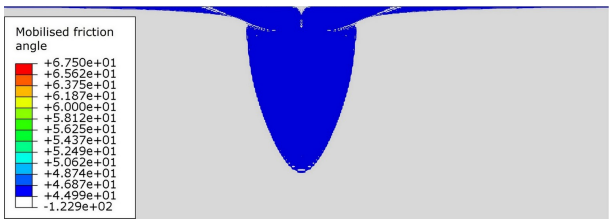

(a) $K_0 = 0.5$.

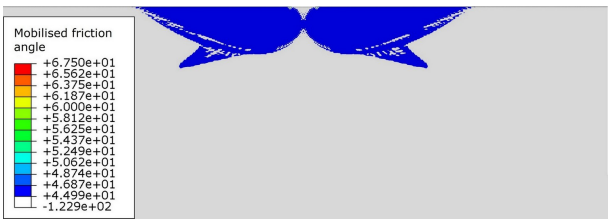

(b) $K_0 = 5$.

Figure 10: Comparison of the mobilised friction angle (expressed in degrees) for the case of soil having $\phi = 45°$ for different levels of earth pressure at rest K_0. Poisson's ratio is assumed equal to 0.4.

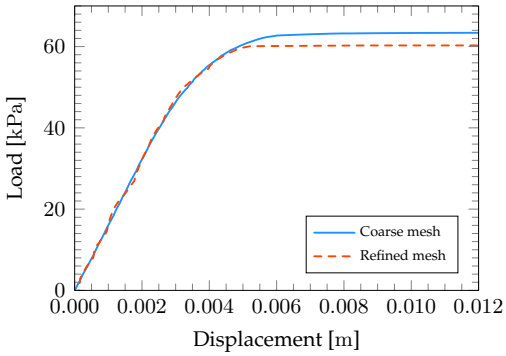

(a) $\phi = 15°$.

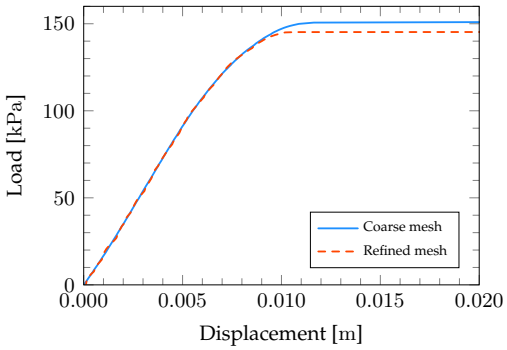

(b) $\phi = 20°$.

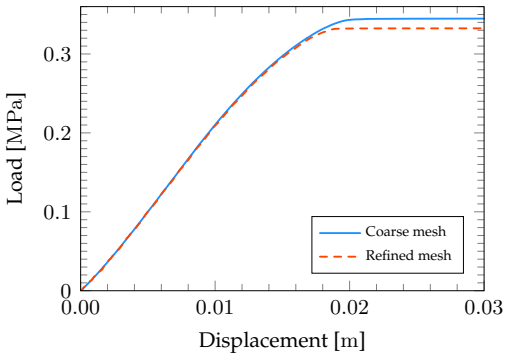

(c) $\phi = 25°$.

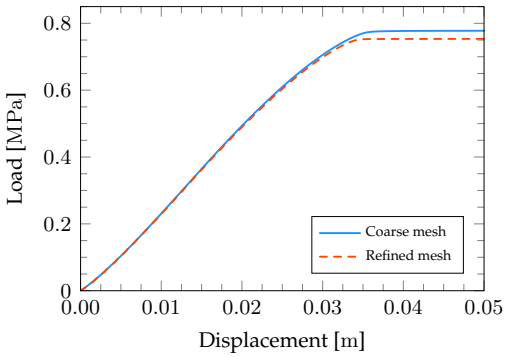

(d) $\phi = 30°$.

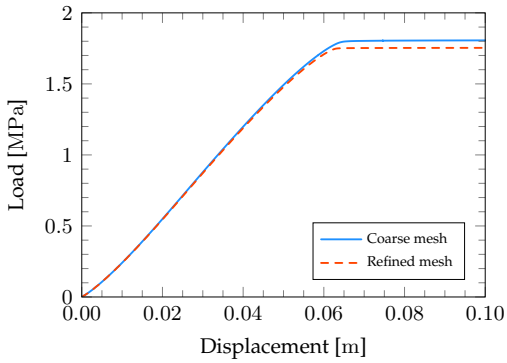

(e) $\phi = 35°$.

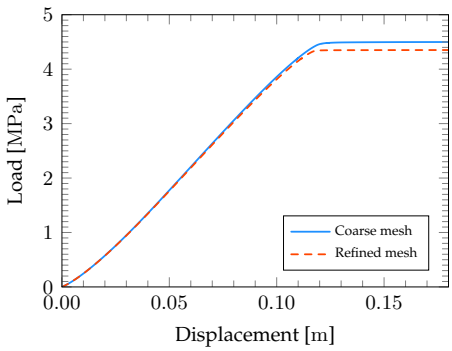

(f) $\phi = 40°$.

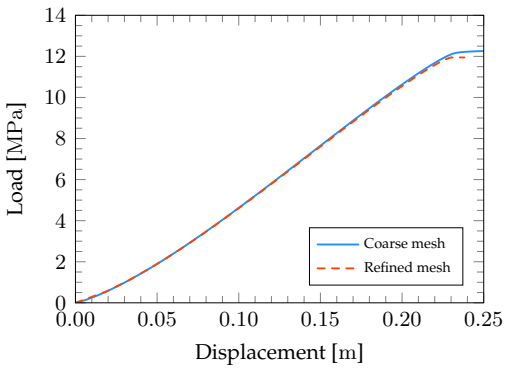

(g) $\phi = 45°$.

Figure 11: Load-displacement curves for the centrally loaded foundation. A comparison is made between a coarse (0.5 m element size, solid line) and a refined (0.2 m element size, dashed line) mesh. Several cases of soil with different internal friction angle are considered.

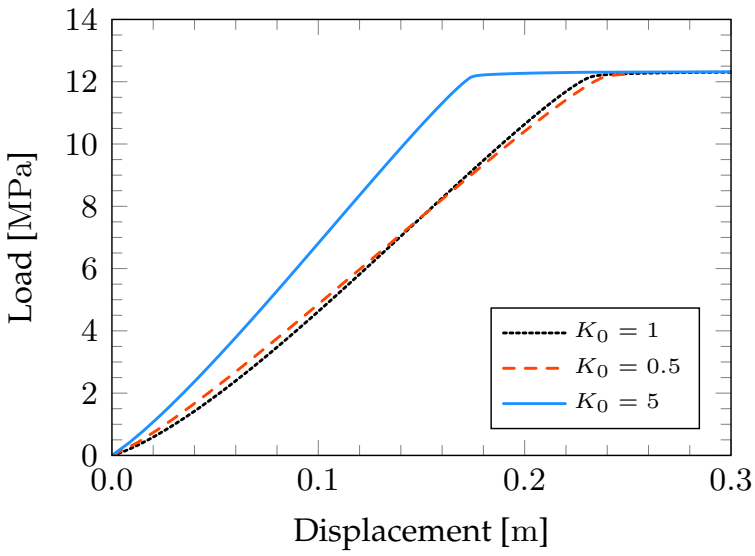

Figure 12: Comparison of the load-displacement curves for the centrally loaded foundation for a soil (internal friction angle equal to 45°) with different coefficient of earth pressure.

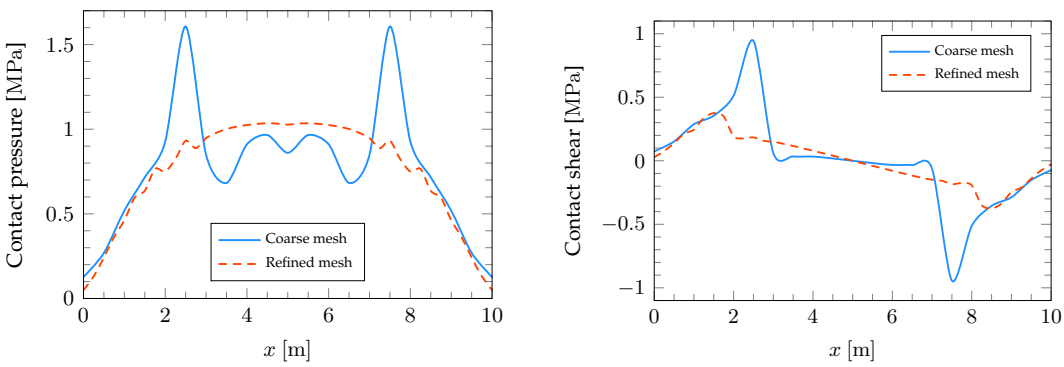

(a) $\phi = 30°$. **(b)** $\phi = 30°$.

Figure 13: Typical contact pressure and shear stress distribution evaluated at the base of the foundation beam when limit load is reached using FEM model with a coarse (0.5 m element size, solid line) and a refined (0.2 m element size, dashed line) mesh.

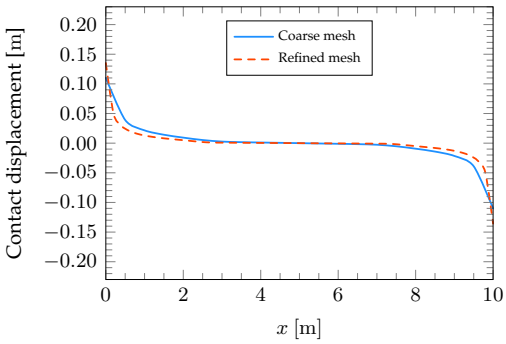

(a) $\phi = 15°$.

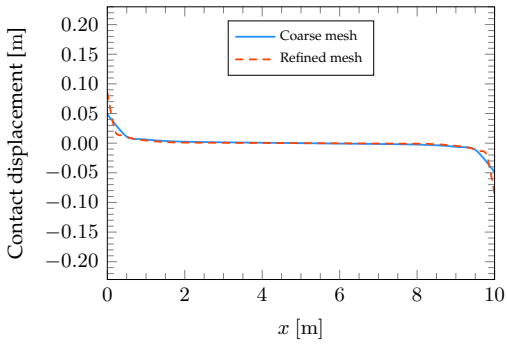

(b) $\phi = 20°$.

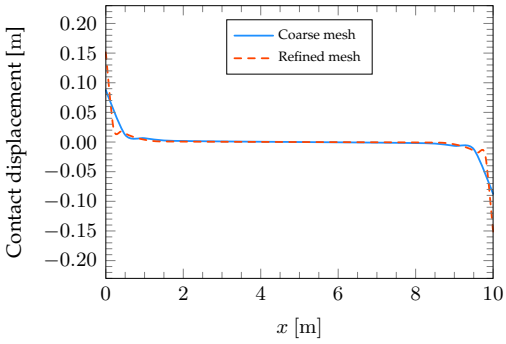

(c) $\phi = 25°$.

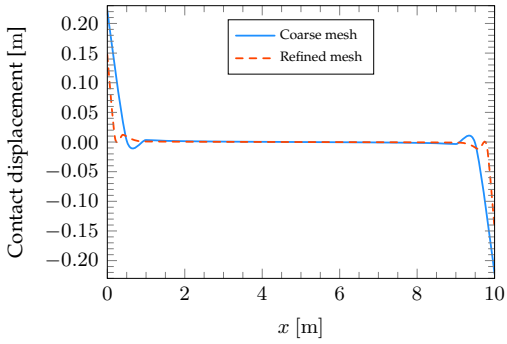

(d) $\phi = 30°$.

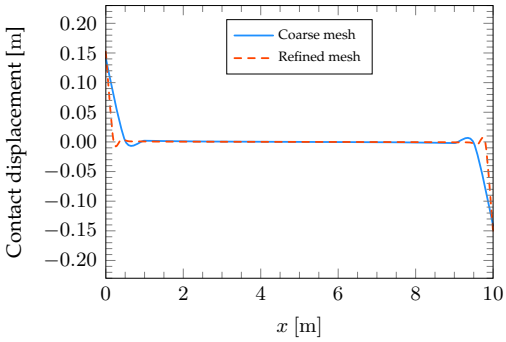

(e) $\phi = 35°$.

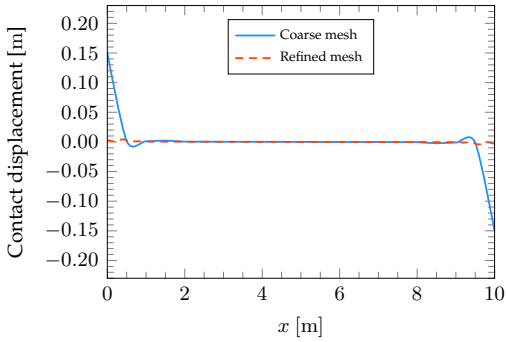

(f) $\phi = 40°$.

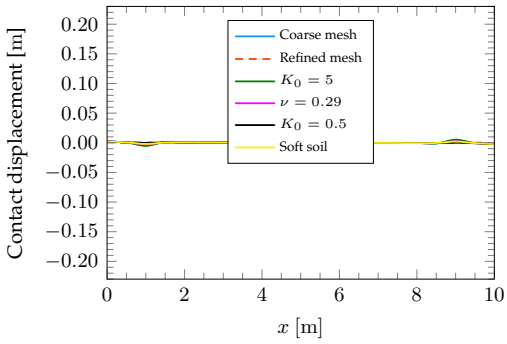

(g) $\phi = 45°$.

Figure 14: Relative displacements at soil-foundation contact evaluated when approaching the limit load using the proposed model. A comparison is made between a coarse (0.5 m element size, solid line) and a refined (0.2 m element size, dashed line) mesh.

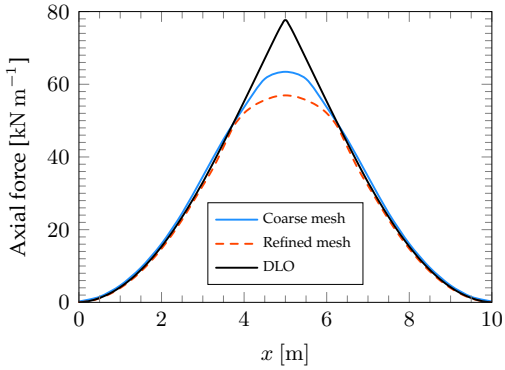

(a) $\phi = 15°$.

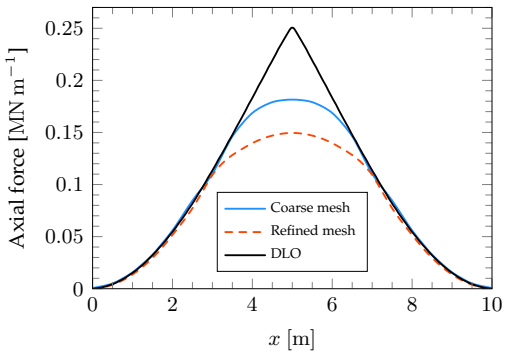

(b) $\phi = 20°$.

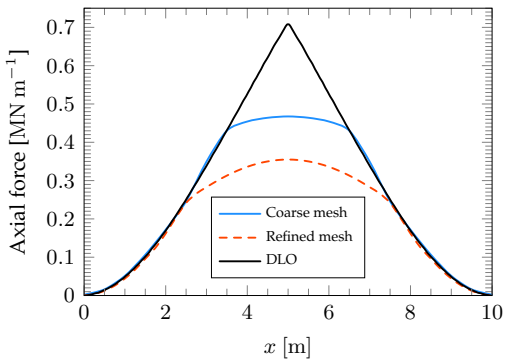

(c) $\phi = 25°$.

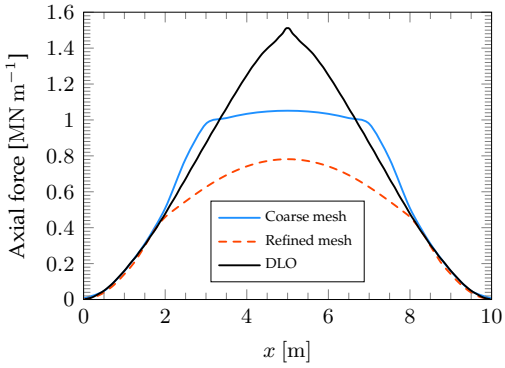

(d) $\phi = 30°$.

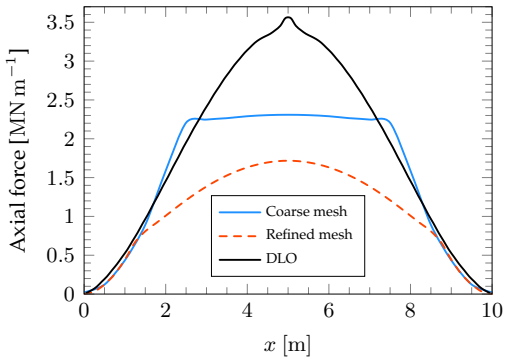

(e) $\phi = 35°$.

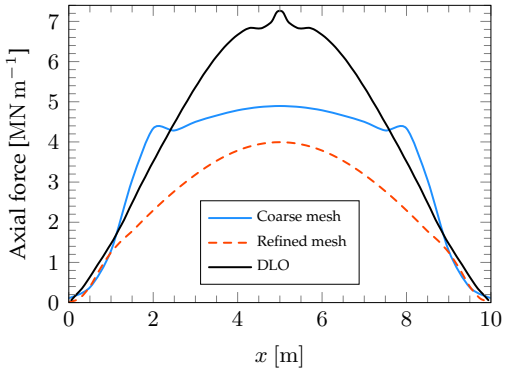

(f) $\phi = 40°$.

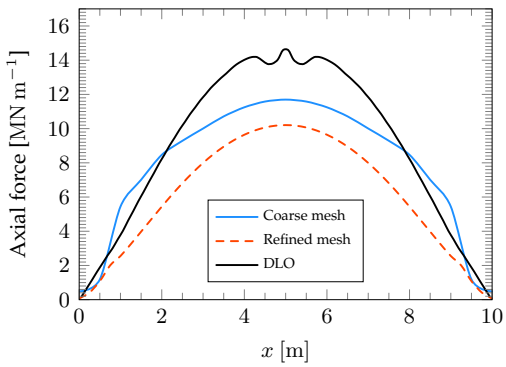

(g) $\phi = 45°$.

Figure 15: Axial force per unit length evaluated along the foundation beam when limit load is reached using the proposed model. A comparison is made between a coarse (0.5 m element size, solid line) and a refined (0.2 m element size, dashed line) mesh.

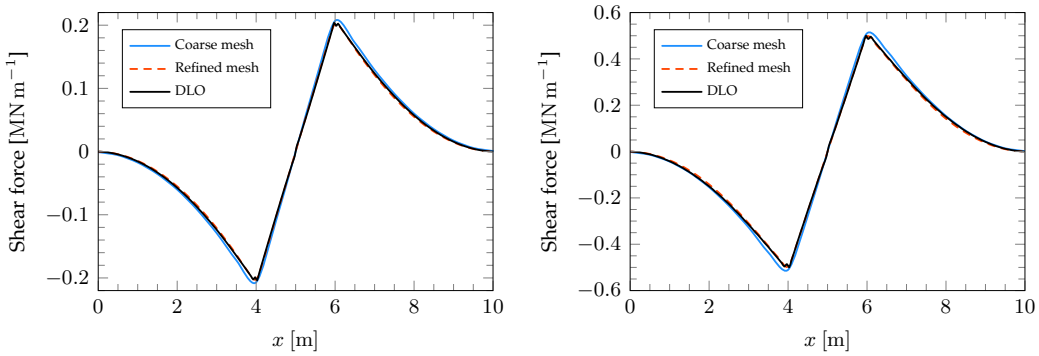

(a) $\phi = 15°$.

(b) $\phi = 20°$.

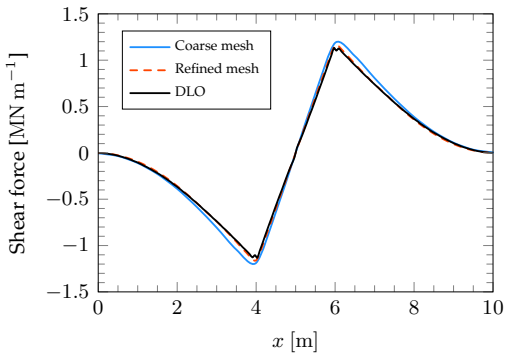

(c) $\phi = 25°$.

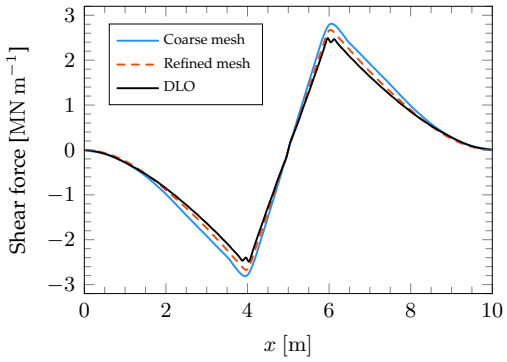

(d) $\phi = 30°$.

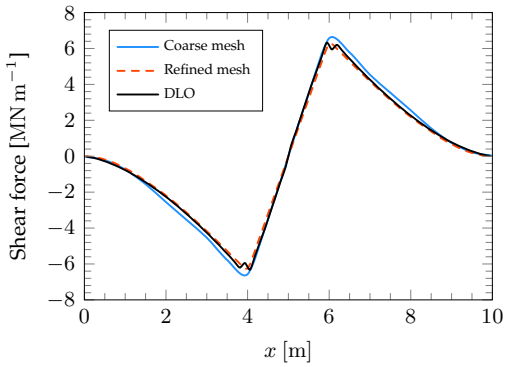

(e) $\phi = 35°$.

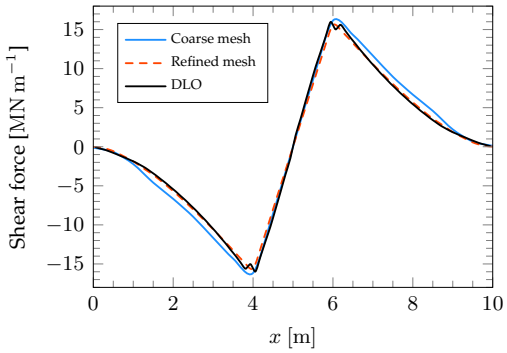

(f) $\phi = 40°$.

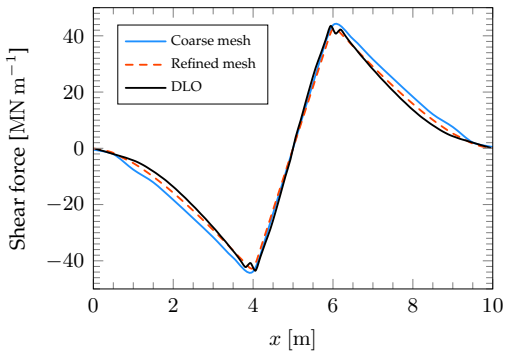

(g) $\phi = 45°$.

Figure 16: Shear force per unit length evaluated along the foundation beam when limit load is reached using the proposed model. A comparison is made between a coarse (0.5 m element size, solid line) and a refined (0.2 m element size, dashed line) mesh.

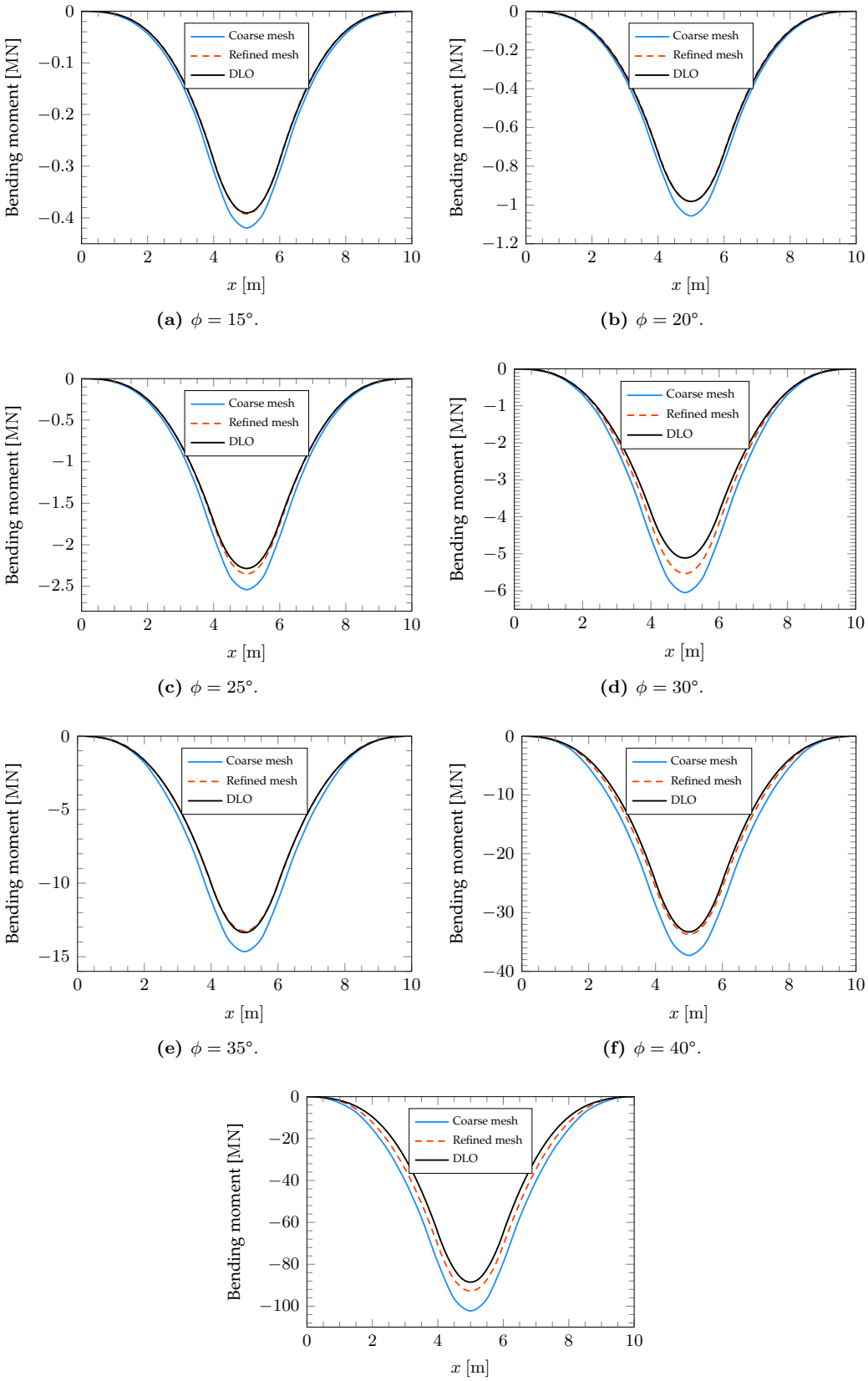

(a) $\phi = 15°$.

(b) $\phi = 20°$.

(c) $\phi = 25°$.

(d) $\phi = 30°$.

(e) $\phi = 35°$.

(f) $\phi = 40°$.

(g) $\phi = 45°$.

Figure 17: Bending moment per unit length evaluated along the foundation beam when limit load is reached using the proposed model. A comparison is made between a coarse (0.5 m element size, solid line) and a refined (0.2 m element size, dashed line) mesh.

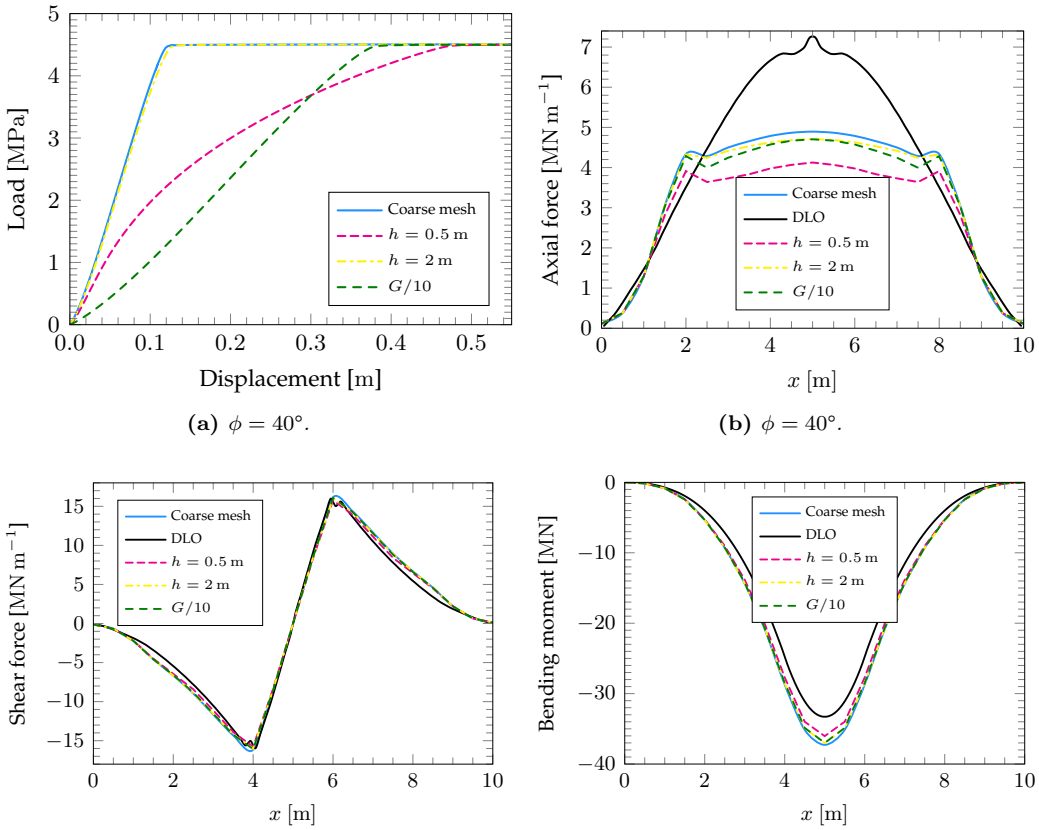

(a) $\phi = 40°$.

(b) $\phi = 40°$.

(c) $\phi = 40°$.

(d) $\phi = 40°$.

Figure 18: Load-displacement curves and beam forces per unit length evaluated along the foundation at the limit load, for different soil ($f = 1$ and $f = 0.1$) and beam stiffnesses ($h = 0.5$ m and $h = 2.0$ m), obtained with coarse mesh (0.5 m element size) and $\phi = 40°$. A comparison is made with DLO results.

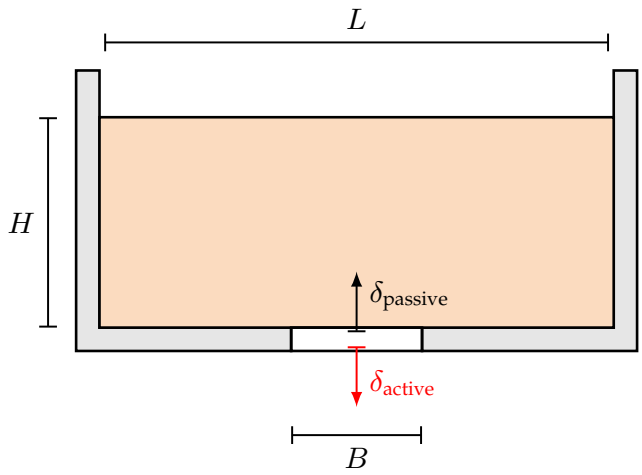

Figure 19: Reference scheme for the trapdoor problem.

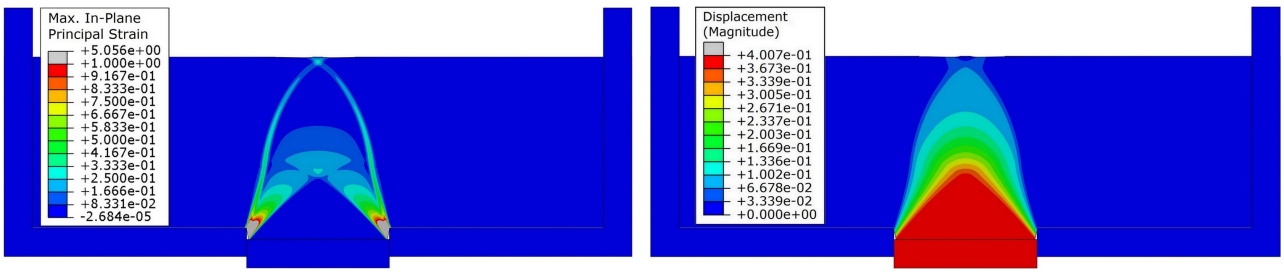

(a) *Strain field for an active trapdoor.*

(b) *Displacement field for an active trapdoor.*

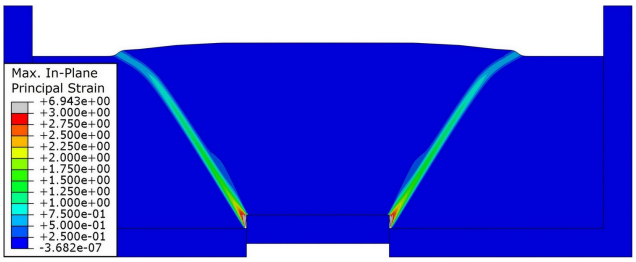

(c) *Strain field for a passive trapdoor.*

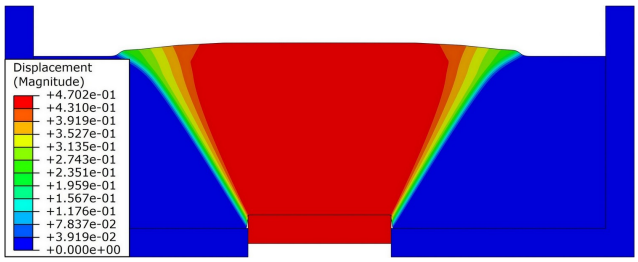

(d) *Displacement field for a passive trapdoor.*

Figure 20: Comparison of the displacement (expressed in metres) and strain fields for the active and passive trapdoor problems. The images are related to the case of a soil with internal friction angle equal to 35° and the aspect ratio of the trapdoor H/B is equal to 1.2.

for larger values FEM results coincide with the upper bound solution. For the active trapdoor problem, FEM results are slightly smaller than the upper bound solution until the H/B ratio is lower than 2.5, whereas for larger values FEM results lay in the range between the lower and upper bound solutions (although they are closer to the upper bound). Moreover, the failure mechanism are consistent with those evaluated by Garcia & Bray and Liang & Xu [9, 15] with discrete element methods (DEM) using the commercial PFC code, and load-displacement curves obtained from FEM simulations (not reported here for the sake of conciseness) are consistent with those obtained from experiments [3, 10] on reduced scale models tested in laboratory.

6. Conclusions

This work proposes and validates a new hyper-elastic formulation which allows to solve the convergence problems and to improve the convergence rate of Mohr-Coulomb-like constitutive models at small stress states that are close to the apex of the yield surface, implying an elastic predictor that can lay in a region in which the yield surface is not defined. The proposed hyper-elastic formulation avoids the occurrence of stress states with tensile mean pressures, following the same approach of the original Cam-Clay hyper-elasticity, and provides shear and bulk stiffnesses increasing with the square root of mean stress, according to the hyper-elastic formulation proposed by Gajo & Bigoni [5]. The proposed formulation is obtained through the combination of two existing formulations: the original Cam-Clay model and Gajo & Bigoni [5] hyper-elasticity model. The resulting free

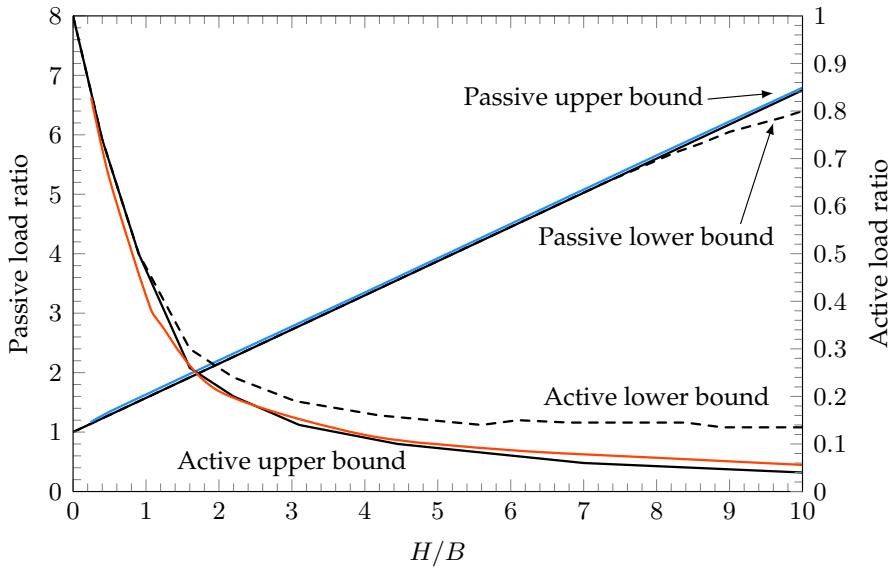

Figure 21: Summary of the limit loads obtained for trapdoor the problem using the proposed model considering active mechanism (shown orange) and passive mechanism (shown blue). A comparison is performed with the solutions obtained with DLO (see Smith [28]).

energy density function is sufficiently smooth to ensure good convergence properties and provides an overall response which captures many typical aspects of granular soil behaviour.

The proposed elasticity model is implemented in a user-defined subroutine (UMAT) for Abaqus Unified FEA (Dassault Systèmes®), using as a plastic driver a C2 continuous approximation of the Mohr-Coulomb yield surface proposed in the literature [1]. An associated flow rule is used and a perfect plasticity is considered.

Model validation is obtained by comparing FEM results with the upper bound computational limit analysis (CLA) method Discontinuity Layout Optimization (DLO) (Smith and Gilbert [30]), with the lower bound solution proposed by Smith [29], and with the results of the characteristic lines method implemented in the ABC program written by Martin [17, 18, 19, 20] for the classical problem of a shallow, centred-loaded, non-yielding foundation. An in-depth comparison of the results obtained from FEM computations with DLO and ABC for the problem of a centred-loaded shallow foundations is performed, showing that structured triangular meshes may lead to wrong (non symmetrical) rupture mechanisms and inaccurate limit loads, whereas unstructured triangular meshes and quadrangular meshes provide reliable evaluations of the limit loads, that typically fall within the range of upper and lower bound solutions. Mesh refinement does not affect significantly the limit load, but it affects the bending moments and in particular the axial forces along the foundation beam. In particular, FEM simulations highlight the partial slippage occurring at lateral sides of the beam foundation, due to the low contact pressures applied close to the foundation corners, and the occurrence of very large axial tensile forces in the central section of the foundation beam. These forces are typically neglected in the current practice of foundation design and, in combination with bending moments, could lead to combined rupture mechanisms involving yielding (both axial resistance and bending resistance can be reached or exceeded) in the foundation and in the soil. These topics will be the subject of a forthcoming work.

In addition, FEM results are compared also with the upper and lower bound solutions proposed by Smith [28] for the active and passive trapdoor problem. In both cases, FEM results are consistent with theoretical solutions, falling within the range of upper and lower bound values. Moreover, the predicted failure mechanism and limit loads are consistent with those found by means of other numerical methods (i.e. DEM) and laboratory experiments.

The proposed elasticity law has however a more general validity than that discussed in this work, because the proposed formulation could be implemented in any classical elastic-plastic constitutive model, based on a Mohr-Coulomb-like yield criterion, thus enhancing model response at small stresses, such as those occurring in many practical applications such as horizontally loaded piles or sheet pile walls.

Appendix A. Coefficients for C2 continuous deviatoric approximation of the Mohr-Coulomb surface

The coefficient C employed for the C2 continuous smoothing of the vertices of the yield surface in the deviatoric section was given by Abbo et al. [1] and is reported below for the sake of completeness as

$$C = C_1 + C_2 \langle \theta \rangle \sin \phi \,, \tag{A.1}$$

where

$$C_1 = -\frac{\cos(3\theta_\mathrm{T})\cos\theta_\mathrm{T} + 3\sin(3\theta_\mathrm{T})\sin\theta_\mathrm{T}}{18\cos^3(3\theta_\mathrm{T})}\,, \tag{A.2a}$$

$$C_2 = \frac{1}{\sqrt{3}}\frac{\cos(3\theta_\mathrm{T})\sin\theta_\mathrm{T} - 3\sin(3\theta_\mathrm{T})\cos\theta_\mathrm{T}}{18\cos^3(3\theta_\mathrm{T})}\,, \tag{A.2b}$$

and the function $\langle\theta\rangle$ is the modified sign function (denoted with angle brackets) of the Lode angle defined as

$$\langle\theta\rangle = \begin{cases} 1 & \text{for } \theta \geq 0\ , \\ -1 & \text{for } \theta < 0\ , \end{cases}\,, \tag{A.3}$$

Similarly, coefficient B can be rewritten in the following form

$$B = B_1\,\langle\theta\rangle + B_2\sin\phi\,, \tag{A.4}$$

in which

$$B_1 = \frac{\cos\theta_\mathrm{T}\ \sin(6\theta_\mathrm{T}) - 6\cos(6\theta_\mathrm{T})\sin\theta_\mathrm{T}}{18\cos^3(3\theta_\mathrm{T})}\,, \tag{A.5a}$$

$$B_2 = -\frac{1}{\sqrt{3}}\frac{\sin\theta_\mathrm{T}\ \sin(6\theta_\mathrm{T}) + 6\cos(6\theta_\mathrm{T})\cos\theta_\mathrm{T}}{18\cos^3(3\theta_\mathrm{T})}\,, \tag{A.5b}$$

whereas coefficient A can be obtained as

$$A = A_1 + A_2\,\langle\theta\rangle\sin\phi\,, \tag{A.6}$$

where

$$A_1 = \cos\theta_\mathrm{T} - B_1\sin(3\theta_\mathrm{T}) - C_1\sin^2(3\theta_\mathrm{T})\,, \tag{A.7a}$$

$$A_2 = -\frac{1}{\sqrt{3}}\sin\theta_\mathrm{T} - B_2\sin(3\theta_\mathrm{T}) - C_2\sin^2(3\theta_\mathrm{T})\,. \tag{A.7b}$$

Declaration of Competing Interest

The authors declare that they have no known competing financial interests or personal relationships that could have appeared to influence the work reported in this paper.

CRediT authorship contribution statement

Luca Prakash Argani: Data curation, Formal analysis, Investigation, Software, Methodology, Visualization; Roles/Writing - original draft; Writing - review & editing. Alessandro Gajo: Conceptualization, Formal analysis, Investigation, Software, Methodology, Roles/Writing - original draft; Writing - review & editing.

Acknowledgements

L.P.A. would like to thank the University of Trento for financial support and provision of excellent research facilities, and gratefully acknowledges resources, support, and research facilities from University of Liverpool and EPSRC (UK).

References

[1] Abbo A.J., Lyamin A.V., Sloan S.W., Hambleton J.P. (2011). A C2 continuous approximation to the Mohr–Coulomb yield surface. International Journal of Solids and Structures, vol. 48, no. 21, pp. 3001-3010. doi: 10.1016/j.ijsolstr.2011.06.021

[2] Abbo A.J., Sloan S.W. (1995). A smooth hyperbolic approximation to the Mohr-Coulomb yield criterion. Computers & Structures, vol. 54, no. 3, pp. 427-441. doi: 10.1016/0045-7949(94)00339-5

[3] Chevalier B., Combe G., Villard P. (2012). Experimental and discrete element modeling studies of the trapdoor problem: influence of the macro-mechanical frictional parameters. Acta Geotechnica, vol. 7, no. 1, pp. 15-39.

[4] Costa Y.D., Zornberg J.G., Bueno B.S., Costa C.L. (2009). Failure Mechanisms in Sand over a Deep Active Trapdoor. Journal of Geotechnical and Geoenvironmental Engineering, vol. 135, no. 11, pp. 1741-1753. doi: 10.1061/(ASCE)GT.1943-5606.0000134

[5] Gajo A., Bigoni D. (2008). A model for stress and plastic strain induced nonlinear, hyperelastic anisotropy in soils. Int. J. Numer. Anal. Meth. Geomech., vol 32, no. 7, pp. 833-861. doi: 10.1002/nag.648

[6] Gajo A., Muir Wood D. (1999). Severn-Trent sand: a kinematic-hardening constitutive model: the *q-p* formulation. Géotechnique, vol 49, no. 5, pp. 595-614. doi: 10.1680/geot.1999.49.5.595

[7] Gajo A., Muir Wood D. (1999). A kinematic hardening constitutive model for sands: the multiaxial formulation. Int. J. Numer. Anal. Meth. Geomech., vol. 23, no. 9, pp. 925-965. doi: 10.1002/(SICI)1096-9853(19990810)23:9<925::AID-NAG19>3.0.CO;2-M

[8] Gajo A., Smith C.C. (2018). Combined rupture mechanisms in shallow foundations. Canadian Geotechnical Journal, vol. 55, no. 6, pp. 829-838. doi: 10.1139/cgj-2016-0324

[9] Garcia F.E., Bray J.D. (2018). Distinct Element Simulations of Shear Rupture in Dilatant Granular Media. Int. J. Geomech., vol. 18, no. 9, pp. 04018111. doi: 10.1061/(ASCE)GM.1943-5622.0001238

[10] Han J., Wang F., Al-Naddaf M., Xu C. (2017). Progressive Development of Two-Dimensional Soil Arching with Displacement. Int. J. Geomech., vol. 17, no. 12, pp. 04017112. doi: 10.1061/(ASCE)GM.1943-5622.0001025

[11] Hardin B.O., Richart E.F.Jr. (1963). Elastic Wave Velocities in Granular Soils. Journal of the Soil Mechanics and Foundation Division, ASCE, vol. 89, no. SM1, pp. 33-65.

[12] Houlsby G.T., Amorosi A., Rojas E. (2005). Elastic moduli of soil dependent on pressure: a hyperelastic formulation. Géotechnique, vol. 55, no. 5, pp. 383-392. doi: 10.1680/geot.2005.55.5.383.

[13] Koutsabeloulis N.C., Griffiths D.V. (1989). Numerical modelling of the trap door problem. Géotechnique, vol. 39, no. 1, pp. 77-89. doi: 10.1680/geot.1989.39.1.77

[14] Lagioia R., Panteghini A. (2015). On the existence of a unique class of yield and failure criteria comprising Tresca, von Mises, Drucker-Prager, Mohr-Coulomb, Galileo-Rankine, Matsuoka-Nakai and Lade-Duncan. Proc. R. Soc. A 472:20150713. doi: 10.1098/rspa.2015.0713

[15] Liang L., Xu C. (2019). Numerical and theoretical research on stress distribution in the loosening zone of the trapdoor problem. Int. J. Numer. Anal. Methods Geomech., vol. 43, no. 7, pp. 1426-1447. doi: 10.1002/nag.2906

[16] Manzari M.T., Dafalias Y.F. (1997). A critical state two-surface plasticity model for sands. Géotechnique, vol 47, no. 2, pp. 255-272. doi: 10.1680/geot.1997.47.2.255

[17] Martin C.M. (2003). User guide for ABC – Analysis of Bearing Capacity, Version 1.0. OUEL Report No. 2261/03. Department of Engineering Science, University of Oxford.

[18] Martin C.M. (2003). New software for rigorous bearing capacity calculations. In Proc. Int. Conf. on Foundations, Dundee, UK, pp. 581–592. London, UK: Thomas Telford.

[19] Martin C.M. (2004). Discussion of "Calculations of bearing capacity factor N_γ using numerical limit analyses" by B. Ukritchon, A.J. Whittle, C. Klangvijit. Journal of Geotechnical and Geoenvironmental Engineering, vol. 130, pp. 1106-1107. doi: 10.1061/(ASCE)1090-0241(2004)130:10(1106)

[20] Martin C.M. (2005). Exact bearing capacity calculations using the method of characteristics. In: Barla G., Barla M., editors. Proceedings of the 11th IACMAG, vol. 4, pp. 441-450.

[21] Ono K., Yamada M. (1993). Analysis of the arching action in granular mass. Géotechnique, vol. 43, no. 1, pp. 105-120. doi: 10.1680/geot.1993.43.1.105

[22] Owen, D.R.J., Hinton, E. (1980). Finite Elements in Plasticity: Theory and Practice. Pineridge Press, Swansea.

[23] Panteghini A., Lagioia R. (2014). A single numerically efficient equation for approximating the Mohr–Coulomb and the Matsuoka–Nakai failure criteria with rounded edges and apex. Int. J. Numer. Anal. Meth. Geomech., vol. 38, no. 4, pp. 349-369. doi: 10.1002/nag.2208

[24] Press W.H., Teukolsky S.A., Vetterling W.T., Flannery B.P. (2007). Numerical Recipes - The Art of Scientific Computing, 3rd Edition. Cambridge University Press. ISBN: 9780521880688.

[25] Rampello S., Tamagnini C., Calabresi G. (1993). Observed and predicted response of a braced excavation in soft to medium clay – Invited Paper. In Predictive Soil Mechanics - Wroth Memorial Symposium, Oxford 1992, Thomas Telford, London: 544-561. ISBN 9780727719164, ISI WOS A1993BY79F00035.

[26] Santichaianaint K. (2002). Centrifuge modeling and analysis of active trapdoor in sand. Ph.D. thesis. Dept. of Civil, Environmental and Architectural Engineering, Univ. of Colorado at Boulder.

[27] Sloan S.W., Booker J.R. (1986). Removal of singularities in Tresca and Mohr-Coulomb yield functions. Commun. Appl. Numer. Methods, vol. 2, no. 2, pp. 173-179. doi: 10.1002/cnm.1630020208

[28] Smith C.C. (1998). Limit loads for an anchor/trapdoor embedded in an associative Coulomb soil. Int. J. Numer. Anal. Meth. Geomech., vol. 22, no. 11, pp. 855-865. doi: 10.1002/(SICI)1096-9853(199811)22:11<855::AID-NAG945>3.0.CO;2-4

[29] Smith C.C. (2005). Complete limiting stress solutions for the bearing capacity of strip footings on a Mohr-Coulomb soil. Géotechnique, vol. 55, no. 8, pp. 607-612. doi: 10.1680/geot.2005.55.8.607

[30] Smith C.C., Gilbert M. (2007). Application of discontinuity layout optimization to plane plsticity problems. Proc. Roy. Soc. A, vol. 463, pp. 2461-2484. doi: 10.1098/rspa.2006.1788

[31] Stone K.J.L., Muir Wood D. (1992). Effects of Dilatancy and Particle Size Observed in Model Tests on Sand. Soils and Foundations, vol. 32, no. 4, pp. 43-57. doi: 10.3208/sandf1972.32.4_43

[32] Taiebat M., Dafalias Y.F. (2008). SANISAND: Simple anisotropic sand plasticity model. Int. J. Numer. Anal. Meth. Geomech., vol. 32, no. 8, pp. 915-948. doi: doi.org/10.1002/nag.651

[33] Terzaghi K. (1936). Stress distribution in dry and saturated sand above a yielding trap-door. Proc., 1st International Conference on Soil Mechanics and Foundation Engineering, Cambridge, Mass., pp. 35-39.

[34] Vairaktaris E., Stavropoulou M. (2013). Modeling of the three-dimensional subsidence diffusion-convection problem above a trapdoor, Int. J. Numer. Anal. Meth. Geomech., vol. 37, no. 6, pp. 551-576. doi: 10.1002/nag.1107

[35] Zhang R., Yang X. (2018). Limit Analysis of Active and Passive Mechanisms of Shallow Tunnels in Nonassociative Soil with Changing Water Table. Int. J. of Geomech., vol. 18, no. 7, pp. 04018063. doi: 10.1061/(ASCE)GM.1943-5622.0001167

[36] Zienkiewicz, O.C., Pande, G.N. (1997). Some useful forms of isotropic yield surfaces for soil and rock mechanics. In: Gudehus, G. (Ed.), Finite Elements in Geomechanics. Wiley, Chichester, pp. 179–190.